Spatial-Temporal Global Sensitivity Analysis for Probabilistic Transient Stability Assessment

Bendong Tan, *Member, IEEE,* Deepjyoti Deka, *Senior Member, IEEE,* and Junbo Zhao, *Senior Member, IEEE*

***Abstract*—With the increasing penetration of intermittent inverter-based resources (IBRs) and flexible loads, identifying critical variables that affect the monitoring and control of stochastic power systems is essential for ensuring secure operation. This paper proposes a hierarchically spatio-temporal global sensitivity analysis framework for probabilistic transient stability assessment (PTSA), capable of quantifying the temporal and spatial sensitivity to correlated uncertain sources, such as IBRs and loads, for correlated generator rotor angle dynamics. To accelerate the computation of sensitivity indices, a computationally efficient surrogate model, i.e., a multi-output Gaussian process emulator (MOGPE), is further developed to replace the time-consuming time-domain simulator used in PTSA. Numerical results on the modified IEEE 9-bus system and the NPCC 140-bus system demonstrate the accuracy, efficiency, and scalability of the proposed method.**

***Index Terms*—Global sensitivity analysis, inverter-based resources, multi-output Gaussian process emulator, probabilistic transient stability assessment, spatiotemporal analysis.**

I. Introduction

THE growing integration of inverter-based resources (IBRs), such as photovoltaic (PV) and wind generation, is transforming the electric grid into a low-inertia system [1], [2]. The increased stochasticity and uncertainty arising from these IBRs and flexible loads further pose significant challenges to the stable operation of power systems. Since traditional deterministic transient stability analysis methods cannot comprehensively show the characteristics of stochastic power systems, probabilistic transient stability assessment (PTSA) has been developed to determine the transient stability level in the presence of uncertain sources [3]–[7].

PTSA aims to quantify how uncertainties propagate from various sources to transient stability. However, the analysis becomes computationally prohibitive when handling numerous uncertainty sources; on the other hand, modeling all potential uncertainties is unnecessary, as some exhibit negligible influence on stability outcomes [8]. Consequently, identifying dominant uncertainty sources can be beneficial in optimizing resource allocation, improving operational efficiency, and establishing clearer input-output causality for PTSA [9].

Sensitivity analysis (SA) quantifies the relative impact of uncertain sources on system outputs by evaluating how input variations propagate through the system. SA methodologies fall into two categories: local sensitivity analysis (LSA) and global sensitivity analysis (GSA) [8], [10], [11]. LSA computes derivatives or finite differences at a nominal operating point to assess the effect of small input perturbations, but it ignores nonlinearities, variable interactions, and global input variations. In contrast, GSA evaluates input influences across the entire input space, accounting for nonlinear effects, higher-order interactions, and individual contributions [12]. This holistic approach makes GSA particularly advantageous for high-dimensional power systems, where comprehensive uncertainty characterization is critical for sensitivity assessment [13], [14].

GSA employs three main methodologies: nonparametric, density-based, and variance-based approaches [8]. Among them, the variance-based method is most commonly used in practice due to its ability to handle nonlinear systems and explicitly decompose sensitivity contributions through hierarchical variance decomposition. This approach relies on Monte Carlo sampling (MCS) [15] to statistically quantify the output variance induced by input uncertainties, enabling simultaneous evaluation of both individual and interactive effects. However, MCS is computationally prohibitive, especially for dynamic simulations, as it requires sampling the power system simulator thousands of times for each input dimension. Although a double-loop generalized unscented transform-based strategy is developed in [16] to alleviate the sampling burden of MCS, it remains time-consuming. This is because the required number of samples grows quadratically with the input dimension.

Consequently, computationally efficient surrogate models have been developed to replace the power system simulator and accelerate computation. Specifically, [13] applied polynomial chaos expansion (PCE) to conduct GSA of correlated uncertain sources, such as load, PV, and wind power, reducing the computational burden compared to a power system simulator. [17] further developed a basis-adaptive sparse polynomial chaos (BASPC) method to alleviate the computational burden of constructing a full PCE while achieving the decomposition of uncorrelated and correlated uncertain sources. [18] extended this approach by developing a BASPC-based GSA scheme that decomposes the sensitivity index into uncorrelated marginal contribution, data correlation contribution and physical interaction contribution. Meanwhile, [19] expanded the work in [17] to multi-output scenarios, where the sensitivity of distributed generations to electrical quantities, such as bus voltages at different locations, is aggregated. To address the curse of dimensionality in PCE and its variants, Gaussian process (GP) and Deep Gaussian process (DGP) were employed in

This work is partially supported by the U.S. National Science Foundation under grants 2442160 and 2328241, and U.S. Department of Energy Office of Electricity (Corresponding author: Junbo Zhao).

B. Tan is with the Department of Electrical and Computer Engineering, University of Connecticut, Storrs, CT. J. Zhao is with Thayer School of Engineering, Dartmouth College, Hanover, NH. D. Deka is with the MIT Energy Initiative, Cambridge, MA. (email: tbd1475141818@gmail.com, junbo.zhao@dartmouth.edu, deepj87@mit.edu)

[20]–[22], respectively, t
distribution system volta
and PVs are involved.

However, current surr
dominantly target steady
able) analyses [13], [17]
sion to multi-output and
critical distinctions are t
1. *Output dimensionality*
metrics (e.g., single bus
different locations. Dyna
tiple outputs, would intro
puts (e.g., post-fault roto
This would require ana
dimensionality;
2. *Computational intens*
significantly higher comp
evaluations, with dynam
simulations per input dir

The authors of [19] have proposed a GSA framework for steady-state multiple outputs, aggregating outputs such as bus voltages at different locations without considering their correlations. However, the method does not generalize to temporally dependent outputs that arise in dynamic multi-output GSA [23]. Furthermore, it requires a prohibitively large sample size to reliably extract principal components, even in the steady-state regime [24]. Therefore, two key research questions remain: *1) How can comprehensive GSA indices be formulated to effectively characterize the impacts of correlated uncertain sources on the dynamic responses in PTSA? 2) How can these GSA indices be efficiently computed, given the computational burden imposed by time-consuming time-domain simulations?*

To address the aforementioned challenges, this paper proposes a hierarchical spatio-temporal GSA method for PTSA. The main contributions are summarized as follows:

- Novel GSA indices are developed to capture the correlations among high-dimensional inputs and temporal outputs. These indices enable an accurate quantification of the relative importance of various uncertainty sources and their physical interactions on power system dynamic responses.
- A computationally efficient surrogate model, termed as the Multi-Output Gaussian Process Emulator (MOGPE), is designed to significantly accelerate the otherwise time-consuming time-domain simulations.
- To the best of our knowledge, this is the first work to establish a comprehensive and interpretable hierarchical spatio-temporal sensitivity analysis framework for PTSA. The proposed method quantifies temporal, spatial, and system-level sensitivities from uncertain sources to generator rotor angle dynamics, supporting the identification of critical uncertainty sources and improving the understanding of uncertainty propagation in PTSA.

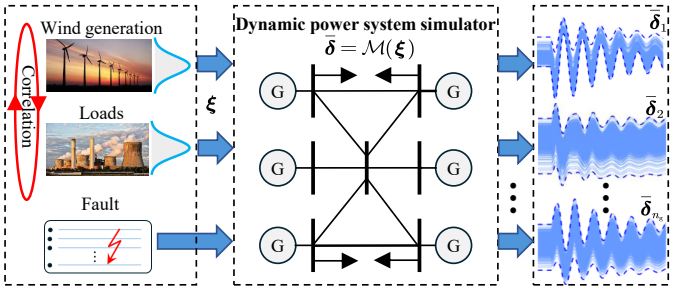

Fig. 1. Problem formulation of PTSA

II. Problem Statement

In PTSA, dynamics are commonly characterized by a system of differential-algebraic equations (DAEs) expressed as:

$$\begin{cases} \dot{\boldsymbol{x}} = \boldsymbol{f}(\boldsymbol{x}, \boldsymbol{y}, \boldsymbol{d}, \boldsymbol{\xi}) \\ \mathbf{0} = \boldsymbol{h}(\boldsymbol{x}, \boldsymbol{y}, \boldsymbol{d}, \boldsymbol{\xi}) \end{cases}, \tag{1}$$

where $\boldsymbol{x}$ denotes the state variables (e.g., generator rotor angles), $\boldsymbol{y}$ represents the algebraic variables (e.g., bus voltage magnitudes), $\boldsymbol{d}$ signifies constant exogenous inputs, i.e., disturbances, and $\boldsymbol{\xi} \in \mathbb{R}^{1\times n_{\mathrm{u}}}$ characterizes n_{u} correlated uncertainty sources, i.e., wind generation and loads in this paper. The nonlinear functions $\boldsymbol{f}(\cdot)$ and $\boldsymbol{h}(\cdot)$ describe the dynamics and algebraic constraints governing the power system.

Applying the backward Euler method to discretize (1) yields:

$$\begin{cases} \boldsymbol{x}(t) = \boldsymbol{x}(t-\Delta t) + \Delta t \times \boldsymbol{f}(\boldsymbol{x}(t), \boldsymbol{y}(t), \boldsymbol{d}, \boldsymbol{\xi}) \\ \mathbf{0} = \boldsymbol{h}(\boldsymbol{x}(t), \boldsymbol{y}(t), \boldsymbol{d}, \boldsymbol{\xi}) \end{cases}, \tag{2}$$

where Δt denotes the time step. (2) can be compactly expressed using an implicit function $\boldsymbol{\mathcal{M}}_t$:

$$\boldsymbol{x}(t) = \boldsymbol{\mathcal{M}}_t(\boldsymbol{x}(t-\Delta t), \boldsymbol{d}, \boldsymbol{\xi}). \tag{3}$$

Through recursive composition, the multi-step formulation emerges:

$$\boldsymbol{x}(t) = \boldsymbol{\mathcal{M}}_t \circ \boldsymbol{\mathcal{M}}_{t-\Delta t} \circ \cdots \circ \boldsymbol{\mathcal{M}}_{t_c+\Delta t}(\boldsymbol{x}(t_c), \boldsymbol{d}, \boldsymbol{\xi}), \tag{4}$$

where t_c denotes the fault inception time and $\circ$ represents function composition. In (4), if $\boldsymbol{d}$ is fixed, then $\boldsymbol{x}(t_c)$ depends on $\boldsymbol{x}(0)$, which is determined by the loading conditions governed by $\boldsymbol{\xi}$. Therefore, $\boldsymbol{x}(t_c)$ is uniquely determined by $\boldsymbol{d}$ and $\boldsymbol{\xi}$. As PTSA focuses on analyzing the evolution of rotor angle $\boldsymbol{\delta} \subset \boldsymbol{x}$ under uncertain $\boldsymbol{\xi}$ for a given $\boldsymbol{d}$, (4) can be rewritten in the compact form:

$$\underbrace{\left[\boldsymbol{\delta}(t_c+\Delta t), \cdots, \boldsymbol{\delta}(t_c+T\Delta t)\right]^\top}_{\overline{\boldsymbol{\delta}} \in \mathbb{R}^{n_{\mathrm{g}}\times T}} = \boldsymbol{\mathcal{M}}(\boldsymbol{\xi}), \tag{5}$$

where t_c denotes the fault clearing time, and $\overline{\boldsymbol{\delta}} = \left[\overline{\boldsymbol{\delta}}_1^\top, \overline{\boldsymbol{\delta}}_2^\top, \cdots, \overline{\boldsymbol{\delta}}_{n_{\mathrm{g}}}^\top\right]^\top$ represents the post-fault rotor angle trajectories of n_{g} generators. For example, $\overline{\boldsymbol{\delta}}_2$ denotes the post-fault rotor angle trajectory of the second generator. $\boldsymbol{\mathcal{M}}(\cdot)$ represents the functional relationship between $\boldsymbol{\xi}$ and $\overline{\boldsymbol{\delta}}$. Given that the uncertain sources $\boldsymbol{\xi} = \left[\boldsymbol{P}_{\mathrm{W}}, \boldsymbol{P}_{\mathrm{L}}\right]^\top$ exhibit diverse probability distributions, the rotor angle trajectory matrix $\overline{\boldsymbol{\delta}}$ inherits a corresponding statistical distribution as uncertainties propagate through the nonlinear function $\boldsymbol{\mathcal{M}}(\cdot)$, as illustrated in Fig. 1. Under high penetration of renewable generations, identifying critical uncertainty sources affecting transient stability becomes imperative. While conventional GSA provides a

viable pathway, its application to PTSA is hindered due to the twin challenges of incorporating high-dimensional correlated outputs, and ensuring computational tractability, as mentioned in the Introduction. To address these challenges, this paper proposes a spatial-temporal GSA approach for PTSA, which not only handles high-dimensional correlated outputs but also significantly accelerates computations by developing an efficient multi-output surrogate model.

III. Global Sensitivity Analysis for PTSA

This section introduces several global sensitivity indices that consider both spatial correlations among uncertain sources and temporal dependencies in the dynamic rotor angle outputs of power systems. To efficiently compute these indices, a surrogate model, namely MOGPE, is proposed to replace the time-domain simulator and significantly reduce computational cost. Finally, a hierarchical spatiotemporal GSA framework is developed to systematically identify critical uncertain sources influencing the spatio-temporal dynamics of power systems and to provide deeper insights into their impact on system behavior.

A. Global Sensitivity Analysis for Scalar Output

This subsection introduces the methodology for GSA with correlated inputs, beginning with scalar outputs before extending to multiple correlated outputs in the subsequent subsection.

1) Analytical First-Order and Total Global Sensitivity Index: Let $\bar{\delta}_{i,t}$ denote the t-th temporal component associated with the i-th generator in vector $\bar{\boldsymbol{\delta}}$. The input-output relationship is:

$$\bar{\delta}_{i,t} = \mathcal{M}(\boldsymbol{\xi}) = \mathcal{M}(\xi_1, \xi_2, \ldots, \xi_{n_\mathrm{u}}), \tag{6}$$

where $\mathcal{M}(\cdot)$ represents a specific component of the vector-valued function $\boldsymbol{\mathcal{M}}(\cdot)$, i.e., $\mathcal{M}(\cdot) \subset \boldsymbol{\mathcal{M}}(\cdot)$. For input vector $\boldsymbol{\xi} = [\xi_1, \xi_2, \ldots, \xi_{n_\mathrm{u}}]$, we define:

- A subset of selected inputs, $\boldsymbol{u} = [\xi_{i1}, \ldots, \xi_{is}]$, where $1 \le s < n_\mathrm{u}$.
- The complementary subset, $\boldsymbol{v} = [\xi_{j1}, \ldots, \xi_{jn-s}]$.

Thus, the complete input vector is $\boldsymbol{\xi} = [\boldsymbol{u}, \boldsymbol{v}]$. The total variance of the output is decomposed as [25]:

$$D^{i,t} = \mathbb{V}_{\boldsymbol{u}}\left[\mathbb{E}_{\boldsymbol{v}}[\mathcal{M}(\boldsymbol{u}, \bar{\boldsymbol{v}})]\right] + \mathbb{E}_{\boldsymbol{u}}\left[\mathbb{V}_{\boldsymbol{v}}[\mathcal{M}(\boldsymbol{u}, \bar{\boldsymbol{v}})]\right] = D^{i,t}_{\boldsymbol{u}} + D^{i,t}_{T_{\boldsymbol{v}}}, \tag{7}$$

where $\mathbb{V}[\cdot]$ and $\mathbb{E}[\cdot]$ denote variance and expectation operators. $D^{i,t}_{\boldsymbol{u}}$ and $D^{i,t}_{T_{\boldsymbol{v}}}$ represent variance contributions caused solely by $\boldsymbol{u}$ and by $\boldsymbol{v}$ including its interaction effects, respectively. Variables $\boldsymbol{v}$ and $\bar{\boldsymbol{v}}$ distinguish between random vectors sampled from joint probability distribution $p(\boldsymbol{u}, \boldsymbol{v})$ and those sampled conditionally from $p(\boldsymbol{u}, \bar{\boldsymbol{v}}|\boldsymbol{u})$.

The first-order global sensitivity (GS) index for subset $\boldsymbol{u}$ is:

$$\begin{aligned} S^{i,t}_{\boldsymbol{u}} &= \frac{\mathbb{V}_{\boldsymbol{u}}\left[\mathbb{E}_{\boldsymbol{v}}[\mathcal{M}(\boldsymbol{u}, \bar{\boldsymbol{v}})]\right]}{D^{i,t}} = \frac{D^{i,t}_{\boldsymbol{u}}}{D^{i,t}} \\ &= \frac{1}{D^{i,t}}\left[\int \mathcal{M}(\boldsymbol{u}, \boldsymbol{v}) p(\boldsymbol{u}, \boldsymbol{v}) d\boldsymbol{u} d\boldsymbol{v} \left[\int \mathcal{M}\left(\boldsymbol{u}, \bar{\boldsymbol{v}}'\right) p\left(\bar{\boldsymbol{v}}' \mid \boldsymbol{u}\right)\right.\right. \\ &\left.\left. d\bar{\boldsymbol{v}}' - \int \mathcal{M}\left(\boldsymbol{u}', \boldsymbol{v}'\right) p\left(\boldsymbol{u}', \boldsymbol{v}'\right) d\boldsymbol{u}' d\boldsymbol{v}'\right]\right], \end{aligned} \tag{8}$$

where $(\boldsymbol{u}', \boldsymbol{v}')$ represent integration variables corresponding to independent realizations of the same uncertain sources as $(\boldsymbol{u}, \boldsymbol{v})$. The total GS index for the complementary subset $\boldsymbol{v}$ is:

$$S^{i,t}_{T_{\boldsymbol{v}}} = \frac{\mathbb{E}_{\boldsymbol{u}}\left[\mathbb{V}_{\boldsymbol{v}}[\mathcal{M}(\boldsymbol{u}, \bar{\boldsymbol{v}})]\right]}{D^{i,t}} = \frac{D^{i,t}_{T_{\boldsymbol{v}}}}{D^{i,t}}. \tag{9}$$

For consistency, (9) can be reformulated to quantify the total GS index for subset $\boldsymbol{u}$:

$$\begin{aligned} S^{i,t}_{T_{\boldsymbol{u}}} &= \frac{\mathbb{E}_{\boldsymbol{v}}\left[\mathbb{V}_{\boldsymbol{u}}[\mathcal{M}(\bar{\boldsymbol{u}}, \boldsymbol{v})]\right]}{D^{i,t}} \\ &= \frac{1}{2D^{i,t}} \int \left[\mathcal{M}(\boldsymbol{u}, \boldsymbol{v}) - \mathcal{M}\left(\bar{\boldsymbol{u}}', \boldsymbol{v}\right)\right]^2 p(\boldsymbol{u}, \boldsymbol{v}) \\ &\quad \times p\left(\bar{\boldsymbol{u}}' \mid \boldsymbol{v}\right) d\boldsymbol{u} d\bar{\boldsymbol{u}}' d\boldsymbol{v}. \end{aligned} \tag{10}$$

As a result, normalizing (7) by $D^{i,t}$ yields the following relationship:

$$1 = S^{i,t}_{\boldsymbol{u}} + S^{i,t}_{T_{\boldsymbol{v}}} \text{ or } 1 = S^{i,t}_{\boldsymbol{v}} + S^{i,t}_{T_{\boldsymbol{u}}}. \tag{11}$$

These sensitivity indices quantify the contribution of input subsets to the total output variance. The first-order index $S^{i,t}_{\boldsymbol{u}}$ captures the variance proportion attributed solely to $\boldsymbol{u}$, while $S^{i,t}_{T_{\boldsymbol{u}}}$ reflects $\boldsymbol{u}$'s total contribution, including both its direct effect and physical interaction effects with other variables. If $S^{i,t}_{\boldsymbol{u}}$ is smaller than $S^{i,t}_{T_{\boldsymbol{u}}}$, it indicates positive physical interaction effects; conversely, it implies negative physical interaction effects.

2) Realization of First-Order and Total Global Sensitivity Index: Since $\mathcal{M}(\cdot)$ doesn't have a closed analytical form, directly computing (8) and (10) is not feasible. Instead, MCS can estimate $S^{i,t}_{\boldsymbol{u}}$ and $S^{i,t}_{T_{\boldsymbol{u}}}$ as follows:

$$\begin{cases} S^{i,t}_{\boldsymbol{u}} = \dfrac{\frac{1}{N}\sum_{j=1}^{N} \mathcal{M}(\boldsymbol{u}_j, \boldsymbol{v}_j)\left(\mathcal{M}(\boldsymbol{u}_j, \bar{\boldsymbol{v}}_j) - \mathcal{M}(\boldsymbol{u}'_j, \boldsymbol{v}'_j)\right)}{D^{i,t}}, \\ S^{i,t}_{T_{\boldsymbol{u}}} = \dfrac{\frac{1}{N}\sum_{j=1}^{N}\left(\mathcal{M}(\boldsymbol{u}_j, \boldsymbol{v}_j) - \mathcal{M}(\bar{\boldsymbol{u}}'_j, \boldsymbol{v}_j)\right)^2}{2D^{i,t}}, \end{cases} \tag{12}$$

where $(\boldsymbol{u}_j, \boldsymbol{v}_j)$ is the j-th sample from the MCS process, and N is the total number of samples. Sampling $(\boldsymbol{u}, \boldsymbol{v})$, $(\boldsymbol{u}', \boldsymbol{v}')$, $(\bar{\boldsymbol{u}}', \boldsymbol{v})$, and $(\boldsymbol{u}, \bar{\boldsymbol{v}}')$ directly is tricky due to correlations in $\boldsymbol{\xi}$ and complex distributions. Notably, $(\bar{\boldsymbol{u}}', \boldsymbol{v})$ and $(\boldsymbol{u}, \bar{\boldsymbol{v}}')$ require conditional distribution sampling. Such sampling can be done using a Gaussian Copula [25], defined as:

$$C(\boldsymbol{w}; \mathbf{R}) = \boldsymbol{\Phi}_{\mathcal{N}}\left(\boldsymbol{\Phi}^{-1}(\boldsymbol{w})\right), \tag{13}$$

where $\boldsymbol{w} = [w_1, w_2, \ldots, w_{n_\mathrm{u}}]$ are uniform random variables in $[0, 1]^n$, $\boldsymbol{\Phi}^{-1}$ is the inverse CDF of an uncorrelated n-dimensional standard normal distribution, and $\boldsymbol{\Phi}_{\mathcal{N}}$ is the CDF of an n_u-dimensional standard normal distribution with correlation matrix $\mathbf{R}$:

$$\mathbf{R} = \begin{bmatrix} \mathbf{R}_{\boldsymbol{u}} & \mathbf{R}_{\boldsymbol{uv}} \\ \mathbf{R}_{\boldsymbol{vu}} & \mathbf{R}_{\boldsymbol{v}} \end{bmatrix} = \mathbf{L}\mathbf{L}^{\top}, \tag{14}$$

with $\mathbf{L}$ as the Cholesky decomposition of $\mathbf{R}$, and $\mathbf{R}_{\boldsymbol{u}}$ as the correlation block for $\boldsymbol{u}$ (similarly for other blocks). (13) maps any input variable ξ_i to a standard normal distribution via a uniform w_i.

To sample the four pairs $(\boldsymbol{u}, \boldsymbol{v})$ and $(\boldsymbol{u}', \boldsymbol{v}')$ from the joint distribution, and $(\boldsymbol{u}, \bar{\boldsymbol{v}}')$ and $(\bar{\boldsymbol{u}}', \boldsymbol{v})$ from the respective conditional distributions, two independent sets of uniform random variables can be generated: $\boldsymbol{w} = [\boldsymbol{w}_{\boldsymbol{u}}, \boldsymbol{w}_{\boldsymbol{v}}]$ and $\boldsymbol{w}' = [\boldsymbol{w}'_{\boldsymbol{u}}, \boldsymbol{w}'_{\boldsymbol{v}}]$, where:

$$\begin{aligned} \boldsymbol{w}_{\boldsymbol{u}} &= [w_{i1}, \ldots, w_{is}], \quad \boldsymbol{w}_{\boldsymbol{v}} = [w_{j1}, \ldots, w_{jn-s}], \\ \boldsymbol{w}'_{\boldsymbol{u}} &= [w'_{i1}, \ldots, w'_{is}], \quad \boldsymbol{w}'_{\boldsymbol{v}} = [w'_{j1}, \ldots, w'_{jn-s}]. \end{aligned}$$

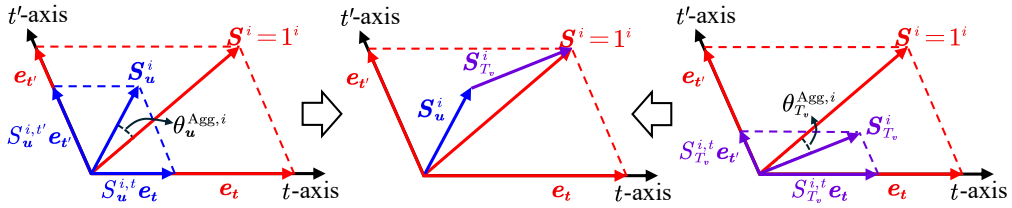

Fig. 2. The relationships among sensitivity vectors if there are only two outputs for i-th generator .

Using the derivation in [25], we have the following properties to generate all necessary samples:

$$\begin{cases} [\boldsymbol{a}, \boldsymbol{b}] = \boldsymbol{\Phi}^{-1}([\boldsymbol{w}_{\boldsymbol{u}}, \boldsymbol{w}_{\boldsymbol{v}}])\mathbf{L}^\top, \\ [\boldsymbol{a}', \boldsymbol{b}'] = \boldsymbol{\Phi}^{-1}([\boldsymbol{w}'_{\boldsymbol{u}}, \boldsymbol{w}'_{\boldsymbol{v}}])\mathbf{L}^\top, \end{cases} \tag{15}$$

$$\begin{cases} \bar{\mathbf{L}}_{\boldsymbol{v}}\bar{\mathbf{L}}_{\boldsymbol{v}}^\top = \mathbf{R}_{\boldsymbol{v}} - \mathbf{R}_{\boldsymbol{vu}}\mathbf{R}_{\boldsymbol{u}}^{-1}\mathbf{R}_{\boldsymbol{uv}}, \\ \bar{\mathbf{L}}_{\boldsymbol{u}}\bar{\mathbf{L}}_{\boldsymbol{u}}^\top = \mathbf{R}_{\boldsymbol{u}} - \mathbf{R}_{\boldsymbol{uv}}\mathbf{R}_{\boldsymbol{v}}^{-1}\mathbf{R}_{\boldsymbol{vu}}, \end{cases} \tag{16}$$

$$\begin{cases} \bar{\boldsymbol{b}}' = \boldsymbol{\Phi}_{\boldsymbol{v}}^{-1}(\boldsymbol{w}'_{\boldsymbol{v}})\bar{\mathbf{L}}_{\boldsymbol{v}}^\top + (\mathbf{R}_{\boldsymbol{vu}}\mathbf{R}_{\boldsymbol{u}}^{-1})^\top \boldsymbol{a}, \\ \bar{\boldsymbol{a}}' = \boldsymbol{\Phi}_{\boldsymbol{u}}^{-1}(\boldsymbol{w}'_{\boldsymbol{u}})\bar{\mathbf{L}}_{\boldsymbol{u}}^\top + (\mathbf{R}_{\boldsymbol{uv}}\mathbf{R}_{\boldsymbol{v}}^{-1})^\top \boldsymbol{b}, \end{cases} \tag{17}$$

$$\begin{cases} (\boldsymbol{u}, \boldsymbol{v}) = \left(\boldsymbol{\Psi}_{\boldsymbol{u}}^{-1}(\boldsymbol{\Phi}(\boldsymbol{a})), \boldsymbol{\Psi}_{\boldsymbol{v}}^{-1}(\boldsymbol{\Phi}(\boldsymbol{b}))\right), \\ (\boldsymbol{u}', \boldsymbol{v}') = \left(\boldsymbol{\Psi}_{\boldsymbol{u}}^{-1}(\boldsymbol{\Phi}(\boldsymbol{a}')), \boldsymbol{\Psi}_{\boldsymbol{v}}^{-1}(\boldsymbol{\Phi}(\boldsymbol{b}'))\right), \\ (\boldsymbol{u}, \bar{\boldsymbol{v}}') = \left(\boldsymbol{\Psi}_{\boldsymbol{u}}^{-1}(\boldsymbol{\Phi}(\boldsymbol{a})), \boldsymbol{\Psi}_{\boldsymbol{v}}^{-1}(\boldsymbol{\Phi}(\bar{\boldsymbol{b}}'))\right), \\ (\bar{\boldsymbol{u}}', \boldsymbol{v}) = \left(\boldsymbol{\Psi}_{\boldsymbol{u}}^{-1}(\boldsymbol{\Phi}(\bar{\boldsymbol{a}}')), \boldsymbol{\Psi}_{\boldsymbol{v}}^{-1}(\boldsymbol{\Phi}(\boldsymbol{b}))\right), \end{cases} \tag{18}$$

where $\boldsymbol{\Phi}_{\boldsymbol{u}}^{-1}$ and $\boldsymbol{\Phi}_{\boldsymbol{v}}^{-1}$ are inverse CDFs of uncorrelated standard normal distributions for $\boldsymbol{u}$ and $\boldsymbol{v}$, and $\boldsymbol{\Psi}_{\boldsymbol{u}}^{-1}$ and $\boldsymbol{\Psi}_{\boldsymbol{v}}^{-1}$ are inverse CDFs of their marginal distributions. For instance:

$$\boldsymbol{\Psi}_{\boldsymbol{u}}^{-1} = [\Psi_{\xi_{i1}}^{-1}, \Psi_{\xi_{i2}}^{-1}, \ldots, \Psi_{\xi_{is}}^{-1}],$$

where $\boldsymbol{\Psi}_{\xi_{ik}}^{-1}$ is the inverse CDF of the k-th component of $\boldsymbol{u}$, with a similar form for $\boldsymbol{\Psi}_{\boldsymbol{v}}^{-1}$. The variables $\boldsymbol{a}$, $\boldsymbol{b}$, $\bar{\boldsymbol{a}}'$, and $\bar{\boldsymbol{b}}'$ are intermediate variables introduced during the sampling process.

B. Global Sensitivity Analysis for High-Dimension Outputs

This subsection extends GSA to the multi-output case. The rotor angles of the i-th generator, $\overline{\boldsymbol{\delta}}_i = [\overline{\delta}_{i,t_c+\Delta t}, \cdots, \overline{\delta}_{i,t_c+T\Delta t}]$, exhibit dynamic correlation. Let the correlation matrix of rotor angles for the i-th generator be defined as:

$$[\mathbf{R}_{\overline{\boldsymbol{\delta}}_i}]_{tt'} \coloneqq \rho_{i,tt'}, \tag{19}$$

where $\rho_{i,tt'}$ is the correlation coefficient between outputs at times t and t'. We can construct an affine coordinate system incorporating these correlations [26], comprising T unit directional vectors $\boldsymbol{e}_t \in \mathbb{R}^{T\times 1}, t = 1, \cdots, T$, that satisfy:

$$\boldsymbol{e}_t^\top \boldsymbol{e}_{t'} = [\mathbf{R}_{\overline{\boldsymbol{\delta}}_i}]_{tt'} = \cos(\theta_{i,tt'}) \quad \text{and} \quad \|\boldsymbol{e}_t\|_2 = 1, \tag{20}$$

and $\theta_{i,tt'}$ is the angle between coordinate axes t and t'.

For vectors $\boldsymbol{\alpha} = \sum_{t=1}^T \alpha_t \boldsymbol{e}_t$ and $\boldsymbol{\beta} = \sum_{t=1}^T \beta_t \boldsymbol{e}_t$ in this space, their inner product is linked to the correlation structure:

$$\boldsymbol{\alpha}^\top \boldsymbol{\beta} = \left(\sum_{t=1}^T \alpha_t \boldsymbol{e}_t\right)^\top \left(\sum_{t'=1}^T \beta_{t'} \boldsymbol{e}_{t'}\right) = \boldsymbol{\alpha}^\top \mathbf{R}_{\overline{\boldsymbol{\delta}}_i} \boldsymbol{\beta}. \tag{21}$$

This induces the $\mathbf{R}_{\overline{\boldsymbol{\delta}}_i}$-weighted inner product and norm:

$$\langle \boldsymbol{\alpha}, \boldsymbol{\beta} \rangle_{\mathbf{R}_{\overline{\boldsymbol{\delta}}_i}} \coloneqq \boldsymbol{\alpha}^\top \mathbf{R}_{\overline{\boldsymbol{\delta}}_i} \boldsymbol{\beta}, \quad \|\boldsymbol{\alpha}\|_{\mathbf{R}_{\overline{\boldsymbol{\delta}}_i}} \coloneqq \sqrt{\boldsymbol{\alpha}^\top \mathbf{R}_{\overline{\boldsymbol{\delta}}_i} \boldsymbol{\alpha}}. \tag{22}$$

Based on the above defined affine coordinate system, (11) can be extended into the vector form:

$$\boldsymbol{S}^i = \mathbf{1}^i = \boldsymbol{S}^i_{\boldsymbol{u}} + \boldsymbol{S}^i_{T_{\boldsymbol{v}}} \text{ or } \boldsymbol{S}^i = \mathbf{1}^i = \boldsymbol{S}^i_{\boldsymbol{v}} + \boldsymbol{S}^i_{T_{\boldsymbol{u}}}, \tag{23}$$

where $\mathbf{1}^i = [1, 1, \cdots, 1]^\top$. Therefore, in this coordinate system, sensitivity vectors are expressed as linear combinations of basis vectors: $\boldsymbol{S}^i = \sum_{t=1}^T 1 \cdot \boldsymbol{e}_t$, $\boldsymbol{S}^i_{\boldsymbol{u}} = \sum_{t=1}^T S^{i,t}_{\boldsymbol{u}} \boldsymbol{e}_t$, and $\boldsymbol{S}^i_{T_{\boldsymbol{v}}} = \sum_{t=1}^T S^{i,t}_{T_{\boldsymbol{v}}} \boldsymbol{e}_t$. To better understand the relationship among these sensitivity vectors, consider a simplified case with only two outputs, i.e., two coordinate axes, t and t'. The relationships between the corresponding sensitivity vectors are illustrated in Fig. 2.

To quantify relative contributions of sensitivity vectors to $\mathbf{1}^i$, we project them onto $\mathbf{1}^i$ based on the vector relationship shown in Fig. 2:

$$\begin{cases} \bar{S}^{\text{Agg},i}_{\boldsymbol{u}} = \dfrac{\|\boldsymbol{S}^i_{\boldsymbol{u}}\|_{\mathbf{R}_{\overline{\boldsymbol{\delta}}_i}} \cos\theta^{\text{Agg},i}_{\boldsymbol{u}}}{\|\mathbf{1}^i\|_{\mathbf{R}_{\overline{\boldsymbol{\delta}}_i}}} = \dfrac{\|\boldsymbol{S}^i_{\boldsymbol{u}}\|_{\mathbf{R}_{\overline{\boldsymbol{\delta}}_i}}}{\|\mathbf{1}^i\|_{\mathbf{R}_{\overline{\boldsymbol{\delta}}_i}}} \dfrac{\langle \boldsymbol{S}^i_{\boldsymbol{u}}, \mathbf{1}^i \rangle_{\mathbf{R}_{\overline{\boldsymbol{\delta}}_i}}}{\|\boldsymbol{S}^i_{\boldsymbol{u}}\|_{\mathbf{R}_{\overline{\boldsymbol{\delta}}_i}} \|\mathbf{1}^i\|_{\mathbf{R}_{\overline{\boldsymbol{\delta}}_i}}}, \\ \bar{S}^{\text{Agg},i}_{T_{\boldsymbol{u}}} = \dfrac{\|\boldsymbol{S}^i_{T_{\boldsymbol{v}}}\|_{\mathbf{R}_{\overline{\boldsymbol{\delta}}_i}} \cos\theta^{\text{Agg},i}_{T_{\boldsymbol{v}}}}{\|\mathbf{1}^i\|_{\mathbf{R}_{\overline{\boldsymbol{\delta}}_i}}} = \dfrac{\|\boldsymbol{S}^i_{T_{\boldsymbol{v}}}\|_{\mathbf{R}_{\overline{\boldsymbol{\delta}}_i}}}{\|\mathbf{1}^i\|_{\mathbf{R}_{\overline{\boldsymbol{\delta}}_i}}} \dfrac{\langle \boldsymbol{S}^i_{T_{\boldsymbol{v}}}, \mathbf{1}^i \rangle_{\mathbf{R}_{\overline{\boldsymbol{\delta}}_i}}}{\|\boldsymbol{S}^i_{T_{\boldsymbol{v}}}\|_{\mathbf{R}_{\overline{\boldsymbol{\delta}}_i}} \|\mathbf{1}^i\|_{\mathbf{R}_{\overline{\boldsymbol{\delta}}_i}}}, \end{cases} \tag{24}$$

where $\theta^{\text{Agg},i}_{\boldsymbol{u}}$ and $\theta^{\text{Agg},i}_{T_{\boldsymbol{v}}}$ are the angles between respective sensitivity vectors and $\mathbf{1}^i$. The indices $\bar{S}^{\text{Agg},i}_{\boldsymbol{u}}$ and $\bar{S}^{\text{Agg},i}_{T_{\boldsymbol{v}}}$ represent the aggregated first-order and total GS indices, measuring the sensitivity of uncertain parameters to the rotor angle trajectory of the i-th generator. Based on the complementarity between $\boldsymbol{u}$ and $\boldsymbol{v}$, and in accordance with (24), we obtain:

$$\begin{cases} \bar{S}^{\text{Agg},i}_{\boldsymbol{u}} = \dfrac{(\boldsymbol{S}^i_{\boldsymbol{u}})^\top \mathbf{R}_{\overline{\boldsymbol{\delta}}_i} \mathbf{1}^i}{(\mathbf{1}^i)^\top \mathbf{R}_{\overline{\boldsymbol{\delta}}_i} \mathbf{1}^i}, \\ \bar{S}^{\text{Agg},i}_{T_{\boldsymbol{v}}} = \dfrac{(\boldsymbol{S}^i_{T_{\boldsymbol{v}}})^\top \mathbf{R}_{\overline{\boldsymbol{\delta}}_i} \mathbf{1}^i}{(\mathbf{1}^i)^\top \mathbf{R}_{\overline{\boldsymbol{\delta}}_i} \mathbf{1}^i}, \end{cases} \text{or} \begin{cases} \bar{S}^{\text{Agg},i}_{\boldsymbol{v}} = \dfrac{(\boldsymbol{S}^i_{\boldsymbol{v}})^\top \mathbf{R}_{\overline{\boldsymbol{\delta}}_i} \mathbf{1}^i}{(\mathbf{1}^i)^\top \mathbf{R}_{\overline{\boldsymbol{\delta}}_i} \mathbf{1}^i}, \\ \bar{S}^{\text{Agg},i}_{T_{\boldsymbol{u}}} = \dfrac{(\boldsymbol{S}^i_{T_{\boldsymbol{u}}})^\top \mathbf{R}_{\overline{\boldsymbol{\delta}}_i} \mathbf{1}^i}{(\mathbf{1}^i)^\top \mathbf{R}_{\overline{\boldsymbol{\delta}}_i} \mathbf{1}^i}. \end{cases} \tag{25}$$

C. Multi-Output Gaussian Process Emulator

As indicated in (12) and (25), computing $S^{i,t}_{\boldsymbol{u}}$, $S^{i,t}_{T_{\boldsymbol{u}}}$, $\bar{S}^{\text{Agg},i}_{\boldsymbol{u}}$ and $\bar{S}^{\text{Agg},i}_{T_{\boldsymbol{u}}}$ for each input dimension requires invoking the time-domain simulator $4N$ times, where N is the total number of samples for each input dimension. In other words, conducting the GSA of rotor angles with respect to all uncertain sources demands $4Nn_{\text{u}}$ time-domain simulations. Typically, N is on the order of $\mathcal{O}(10^4)$, implying that even for the standard IEEE 9-bus system, the computational time can exceed one day. To address this computational burden, this subsection introduces a computationally efficient surrogate model, namely MOGPE, which serves as a replacement for the time-domain simulator to expedite the calculation of $\bar{S}^{\text{Agg},i}_{\boldsymbol{u}}$ and $\bar{S}^{\text{Agg},i}_{T_{\boldsymbol{u}}}$. The following sections provide a detailed explanation of the design and implementation of MOGPE.

1) Construction of MOGPE: Consider a dataset $\mathcal{D} = \{\boldsymbol{\xi}^{(i)}, \widetilde{\boldsymbol{\delta}}^{(i)}\}_{i=1}^{N_\mathrm{t}}$, where $\boldsymbol{\xi}^{(i)} \in \mathbb{R}^{n_\mathrm{u}}$ denotes the n_u-dimensional input, and $\widetilde{\boldsymbol{\delta}} = \left[\overline{\boldsymbol{\delta}}_1, \overline{\boldsymbol{\delta}}_2, \ldots, \overline{\boldsymbol{\delta}}_{n_\mathrm{g}}\right] =\in \mathbb{R}^{1\times n_\mathrm{g}T}$ denotes the $n_\mathrm{g}T$-dimensional output, with N_t data points in total. The output matrix is defined as $\mathbf{Y} = [\mathbf{Y}_{[1]}, \ldots, \mathbf{Y}_{[n_\mathrm{g}T]}] = \{\widetilde{\boldsymbol{\delta}}^{(i)}\}_{i=1}^{N_\mathrm{t}} \in \mathbb{R}^{N_\mathrm{t}\times n_\mathrm{g}T}$, where $\mathbf{Y}_{[j]} \in \mathbb{R}^{N_\mathrm{t}\times 1}$ represents the j-th output across all samples. The corresponding input set is given by $\mathbf{X} = \{\boldsymbol{\xi}^{(i)}\}_{i=1}^{N_\mathrm{t}}$.

Each output dimension can be modeled as a Gaussian process. By definition, any finite collection of function values $g(\cdot)$ follows a joint Gaussian distribution [27]:

$$\boldsymbol{g}(\mathbf{X}) = [g(\boldsymbol{\xi}^{(1)}), \ldots, g(\boldsymbol{\xi}^{(N_\mathrm{t})})]^\top \sim \mathcal{N}(\boldsymbol{\mu}, K_{\mathbf{X},\mathbf{X}}), \tag{26}$$

where the mean function is defined as $\boldsymbol{\mu} = \mathbf{H}(\mathbf{X})\boldsymbol{\beta}$, and $\mathbf{H}(\mathbf{X}) \in \mathbb{R}^{N_\mathrm{t}\times n_\mathrm{p}}$ denotes a set of basis functions. For the i-th input sample $\boldsymbol{\xi}^{(i)} = [\xi_1^{(i)}, \ldots, \xi_{n_\mathrm{u}}^{(i)}]$, the k-th element is denoted by $\xi_k^{(i)}$, where $k = 1, 2, \ldots, n_\mathrm{u}$. A constant basis can be defined as $\mathbf{H}(\boldsymbol{\xi}^{(i)}) = 1$, corresponding to $n_\mathrm{p} = 1$, while a linear basis can be defined as $\mathbf{H}(\boldsymbol{\xi}^{(i)}) = [1, \xi_1^{(i)}, \ldots, \xi_{n_\mathrm{u}}^{(i)}]$, giving $n_\mathrm{p} = 1 + n_\mathrm{u}$, with $\boldsymbol{\beta}$ representing a vector of hyperparameters. The covariance matrix is given by:

$$K_{\mathbf{X},\mathbf{X}} = \begin{bmatrix} k(\boldsymbol{\xi}^{(1)}, \boldsymbol{\xi}^{(1)}) & \cdots & k(\boldsymbol{\xi}^{(1)}, \boldsymbol{\xi}^{(N_\mathrm{t})}) \\ \vdots & \ddots & \vdots \\ k(\boldsymbol{\xi}^{(N_\mathrm{t})}, \boldsymbol{\xi}^{(1)}) & \cdots & k(\boldsymbol{\xi}^{(N_\mathrm{t})}, \boldsymbol{\xi}^{(N_\mathrm{t})}) \end{bmatrix}, \tag{27}$$

where the kernel function is $k(\boldsymbol{\xi}, \boldsymbol{\xi}') = \exp\left(-\frac{1}{2}\left\|\boldsymbol{\xi} - \boldsymbol{\xi}'\right\|^2/\ell^2\right)$ with ℓ denoting the length-scale hyperparameter.

Assuming the observations consist of the latent function corrupted by additive Gaussian noise, the observation model becomes:

$$\mathbf{Y} \sim \mathcal{N}\left(\mathbf{H}\boldsymbol{\beta}, \widetilde{K}\right), \tag{28}$$

where $\widetilde{K} = K_{\mathbf{X},\mathbf{X}} + \sigma^2\mathbf{I}_{N_\mathrm{t}}$. Here, σ^2 denotes the noise variance, and $\mathbf{I}_{N_\mathrm{t}}$ is the $N_\mathrm{t} \times N_\mathrm{t}$ identity matrix.

Modeling each output dimension independently would require constructing $n_\mathrm{g}T$ covariance matrices, each of size $N_\mathrm{t} \times N_\mathrm{t}$, resulting in considerable computational cost. To mitigate this, MOGPE models each output as a Gaussian process, potentially sharing a common covariance structure across inputs while allowing each output to have distinct scaling and mean functions. A scaling factor $\boldsymbol{\lambda} = [\lambda_1, \ldots, \lambda_{n_\mathrm{g}T}] \in \mathbb{R}^{1\times n_\mathrm{g}T}$ is introduced to independently control the magnitude of each output. The observation model for the j-th output is:

$$\mathbf{Y}_{[j]} \sim \mathcal{N}\left(\mathbf{H}\boldsymbol{\beta}_{[j]}\lambda_j, \lambda_j^2\widetilde{K}\right), \tag{29}$$

where $\boldsymbol{\beta}_{[j]}$ denotes a vector of hyperparameters in mean function for j-th output.

2) Hyperparameter Optimization for MOGPE: Assuming conditional independence across outputs given the hyperparameters, the joint log-likelihood is:

$$\log P(\mathbf{Y} \mid \mathbf{X}, \boldsymbol{\vartheta}) = \sum_{j=1}^{n_\mathrm{g}T}\left[-\frac{1}{2\lambda_j^2}(\boldsymbol{r}_{[j]})^\top\widetilde{K}^{-1}(\boldsymbol{r}_{[j]}) - \frac{1}{2}\log\left((2\pi)^{N_\mathrm{t}}\lambda_j^{2N_\mathrm{t}}|\widetilde{K}|\right)\right], \tag{30}$$

where $\boldsymbol{\vartheta} = \{\boldsymbol{\beta}, \boldsymbol{\lambda}, \ell, \sigma^2\}$ denotes the set of model hyperparameters, and $\boldsymbol{r}_{[j]} = \mathbf{Y}_{[j]} - \mathbf{H}\boldsymbol{\beta}_{[j]}\lambda_j$ represents the residual for the j-th output dimension. $\boldsymbol{\vartheta}$, σ^2, and λ_j can be optimized by minimizing $-\log P(\mathbf{Y} \mid \mathbf{X}, \boldsymbol{\vartheta})$ using gradient descent. Given $\boldsymbol{\vartheta}$, σ^2, and λ_j, the optimal $\boldsymbol{\beta}_{[j]}$ is obtained as:

$$\hat{\boldsymbol{\beta}}_{[j]} = \frac{1}{\lambda_j}\left[\mathbf{H}^\top\widetilde{K}^{-1}\mathbf{H}\right]^{-1}\mathbf{H}^\top\widetilde{K}^{-1}\mathbf{Y}_{[j]}. \tag{31}$$

The training complexity is $\mathcal{O}(N_\mathrm{t}^3 + n_\mathrm{p}^3 + n_\mathrm{g}TN_\mathrm{t}^2)$.

Remark 1: The training complexity of the MOGPE emulator arises from three main computational components. First, inverting the covariance matrix $\widetilde{\mathbf{K}}$ of size $N_t \times N_t$ requires $\mathcal{O}(N_t^3)$. Second, solving for the polynomial mean coefficients $\boldsymbol{\beta}$ involves inverting the design matrix of size n_p (the number of polynomial basis functions), which contributes $\mathcal{O}(n_p^3)$. Finally, for each of the n_gT outputs, evaluating gradients of $\log P(\mathbf{Y} \mid \mathbf{X}, \boldsymbol{\vartheta})$ requires repeated matrix-vector multiplications with complexity $\mathcal{O}(N_t^2)$, leading to a total of $\mathcal{O}(n_gTN_t^2)$. Combining these contributions, the overall training complexity is $\mathcal{O}(N_t^3 + n_p^3 + n_gTN_t^2)$.

3) Prediction via MOGPE: For new inputs $\mathbf{X}_*$, the joint distribution of training outputs $\mathbf{Y}_{[j]}$ and test outputs $\mathbf{Y}_{[j]*}$ is:

$$\begin{bmatrix}\mathbf{Y}_{[j]} \\ \mathbf{Y}_{[j]*}\end{bmatrix} \sim \mathcal{N}\left(\begin{bmatrix}\mathbf{H}\boldsymbol{\beta}_{[j]}\lambda_j \\ \mathbf{H}_*\boldsymbol{\beta}_{[j]}\lambda_j\end{bmatrix}, \begin{bmatrix}\lambda_j^2\widetilde{K} & \lambda_j^2K_{\mathbf{X},\mathbf{X}_*} \\ \lambda_j^2K_{\mathbf{X}_*,\mathbf{X}} & \lambda_j^2\widetilde{K}_*\end{bmatrix}\right), \tag{32}$$

where $\widetilde{K}_* = K_{\mathbf{X}_*,\mathbf{X}_*} + \sigma^2\mathbf{I}_*$ and $\mathbf{H}_* = \mathbf{H}(\mathbf{X}_*)$. $\mathbf{I}_*$ is the identity matrix with the same size of $K_{\mathbf{X}_*,\mathbf{X}_*}$. Conditioning on $\mathbf{Y}_{[j]}$, the predictive mean for $\mathbf{Y}_{[j]*}$ is:

$$\mathbb{E}[\mathbf{Y}_{[j]*}] = \mathbf{H}(\mathbf{X}_*)\hat{\boldsymbol{\beta}}_{[j]}\lambda_j + K_{\mathbf{X}_*,\mathbf{X}}\widetilde{K}^{-1}\boldsymbol{r}_{[j]}. \tag{33}$$

(33) is employed as the predicted output of the final model, which can be rewritten in the functional form:

$$\overline{\boldsymbol{\delta}} = \widetilde{\boldsymbol{\mathcal{M}}}(\boldsymbol{\xi}) \text{ and } \overline{\delta}_{i,t} = \widetilde{\mathcal{M}}(\boldsymbol{\xi}), \tag{34}$$

where $\widetilde{\boldsymbol{\mathcal{M}}}(\cdot)$ denotes the surrogate model constructed using MOGPE, and $\widetilde{\mathcal{M}}(\cdot)$ represents a specific component of $\widetilde{\boldsymbol{\mathcal{M}}}(\cdot)$. Consequently, (34) replaces (6) in (12) and (25), enabling the calculation of $S_{\boldsymbol{u}}^{i,t}$, $S_{T_{\boldsymbol{u}}}^{i,t}$, $\bar{S}_{\boldsymbol{u}}^{\mathrm{Agg},i}$, and $\bar{S}_{T_{\boldsymbol{u}}}^{\mathrm{Agg},i}$. Thus, (12) can be rewritten as:

$$\begin{cases} S_{\boldsymbol{u}}^{i,t} = \dfrac{\frac{1}{N}\sum_{j=1}^{N}\widetilde{\mathcal{M}}(\boldsymbol{u}_j, \boldsymbol{v}_j)\left(\widetilde{\mathcal{M}}(\boldsymbol{u}_j, \bar{\boldsymbol{v}}_j) - \widetilde{\mathcal{M}}(\boldsymbol{u}'_j, \boldsymbol{v}'_j)\right)}{D^{i,t}}, \\ S_{T_{\boldsymbol{u}}}^{i,t} = \dfrac{\frac{1}{N}\sum_{j=1}^{N}\left(\widetilde{\mathcal{M}}(\boldsymbol{u}_j, \boldsymbol{v}_j) - \widetilde{\mathcal{M}}(\bar{\boldsymbol{u}}'_j, \boldsymbol{v}_j)\right)^2}{2D^{i,t}}. \end{cases} \tag{35}$$

D. Hierarchically Spatial-Temporal Global Sensitivity Analysis Framework

Once $S_{\boldsymbol{u}}^{i,t}$, $S_{T_{\boldsymbol{u}}}^{i,t}$, $\bar{S}_{\boldsymbol{u}}^{\mathrm{Agg},i}$, and $\bar{S}_{T_{\boldsymbol{u}}}^{\mathrm{Agg},i}$ are calculated, they can be utilized to analyze the spatial-temporal global sensitivity for PTSA, as detailed below:

- **Temporal Sensitivity Analysis:** For the i-th generator, the sensitivity of rotor angle dynamics at each time step can be quantified using $S_{\boldsymbol{u}}^{i,t}$ and $S_{T_{\boldsymbol{u}}}^{i,t}$. This helps operators understand how uncertain sources influence the rotor angle response over time.
- **Spatial Sensitivity Analysis:** For all generators, $\bar{S}_{\boldsymbol{u}}^{\mathrm{Agg},i}$ and $\bar{S}_{T_{\boldsymbol{u}}}^{\mathrm{Agg},i}$ identify which uncertain sources exhibit the highest sensitivity to each generator. These insights provide valuable guidance for future planning and allocation of uncertain sources to mitigate transient instability risks.

Although the sensitivity indices $S_{\boldsymbol{u}}^{i,t}$, $S_{T_{\boldsymbol{u}}}^{i,t}$, $\bar{S}_{\boldsymbol{u}}^{\mathrm{Agg},i}$, and $\bar{S}_{T_{\boldsymbol{u}}}^{\mathrm{Agg},i}$ enable detailed sensitivity analysis for the dynamic responses

of each generator at each time step, they do not provide a system-level perspective. To address this limitation, this study further introduces first-order and total sensitivity indices for the transient stability index (TSI), denoted as $\bar{S}_{\boldsymbol{u}}^{\mathrm{TSI}}$ and $\bar{S}_{T_{\boldsymbol{u}}}^{\mathrm{TSI}}$, respectively:

$$\begin{cases} \bar{S}_{\boldsymbol{u}}^{\mathrm{TSI}} = \dfrac{\frac{1}{N}\sum_{j=1}^{N} \mathrm{TSI}(\boldsymbol{u}_j, \boldsymbol{v}_j)\left(\mathrm{TSI}(\boldsymbol{u}_j, \bar{\boldsymbol{v}}_j) - \mathrm{TSI}(\boldsymbol{u}'_j, \boldsymbol{v}'_j)\right)}{D^{\mathrm{TSI}}}, \\ \bar{S}_{T_{\boldsymbol{u}}}^{\mathrm{TSI}} = \dfrac{\frac{1}{N}\sum_{j=1}^{N} \left(\mathrm{TSI}(\boldsymbol{u}_j, \boldsymbol{v}_j) - \mathrm{TSI}(\bar{\boldsymbol{u}}'_j, \boldsymbol{v}_j)\right)^2}{2D^{\mathrm{TSI}}}. \end{cases} \tag{36}$$

Here, D^{TSI} denotes the variance of the TSI, where TSI is defined as $\mathrm{TSI} = 100 \times \frac{360-\delta_{\max}}{360+\delta_{\max}}$, with $\delta_{\max}$ representing the maximum absolute difference in rotor angles between any two generators. This quantity can be efficiently computed using the surrogate model $\widetilde{\boldsymbol{\mathcal{M}}}(\cdot)$.

The comprehensive spatial-temporal global sensitivity analysis framework is implemented through the following steps, as shown in Fig. 3 and Algorithm 1:

- **Step One: Probabilistic Modeling and Data Generation of Uncertain Sources.** The marginal CDFs $\boldsymbol{\Psi}$ of wind speed and loads are estimated from historical data. A Gaussian Copula is employed to capture their joint distribution, incorporating the correlation matrix $\mathbf{R}$. For detailed Copula construction theory, refer to [28]. Synthetic wind power and load data are generated using Latin Hypercube sampling (LHS) based on the identified Copula structure and subsequently simulated in the time domain under specific fault conditions, yielding the training dataset $\mathcal{D} = \{\boldsymbol{\xi}^{(i)}, \widetilde{\boldsymbol{\delta}}^{(i)}\}_{i=1}^{N_{\mathrm{t}}}$.
- **Step Two: Surrogate Modeling.** The dataset $\mathcal{D}$ trains the MOGPE surrogate model. Specifically, (31) is substituted into (30), and $-\log P(\mathbf{Y} \mid \mathbf{X}, \boldsymbol{\vartheta})$ is minimized using gradient descent over n_{t} iterations to optimize ℓ, σ^2, and
- **Sensitivity Analysis.** With the trained MOGPE, $(\boldsymbol{u}, \boldsymbol{v})$, $(\boldsymbol{u}', \boldsymbol{v}')$, $(\boldsymbol{u}, \bar{\boldsymbol{v}}')$, and $(\bar{\boldsymbol{u}}', \boldsymbol{v})$ are sampled via (15)-(18) using MCS, and then fed into (34) to compute the corresponding rotor angle dynamic responses. The response corresponding to $(\boldsymbol{u}, \boldsymbol{v})$ is used to compute $\mathbf{R}_{\bar{\boldsymbol{\delta}}_i}$. Finally, $S_{\boldsymbol{u}}^{i,t}$ and $S_{T_{\boldsymbol{u}}}^{i,t}$ are computed by substituting (34) into (12), while $\bar{S}_{\boldsymbol{u}}^{\mathrm{Agg},i}$ and $\bar{S}_{T_{\boldsymbol{u}}}^{\mathrm{Agg},i}$ are obtained using (25). The system-level sensitivity indices $\bar{S}_{\boldsymbol{u}}^{\mathrm{TSI}}$ and $\bar{S}_{T_{\boldsymbol{u}}}^{\mathrm{TSI}}$ are derived from (36).

  Consequently, the influence of uncertain sources on generator rotor angle responses can be analyzed across each time instant, location, and the overall system stability level, thereby providing insightful indices for subsequent decision-making.

Remark 2: A general use case of the proposed spatial-temporal global sensitivity analysis is provided for understanding power system stability under uncertain conditions:

- At the system level, the analysis identifies which uncertain sources, such as wind or load variations, have significant impacts on overall stability.
- At the generator level, it highlights the synchronous generators that are most sensitive to these dominant uncertainties based on the system-level sensitivity analysis results. This allows operators to pinpoint the key generators that critically influence system stability.
- At the time-instant level, the method reveals how these uncertainties affect local dynamics over time, such as how uncertain sources influence oscillations. This can guide operators to deploy additional oscillation controllers at uncertain sources, such as wind generators or loads, to regulate the key generators identified in the generator-level analysis.

By integrating these insights, operators gain a spatial-temporal

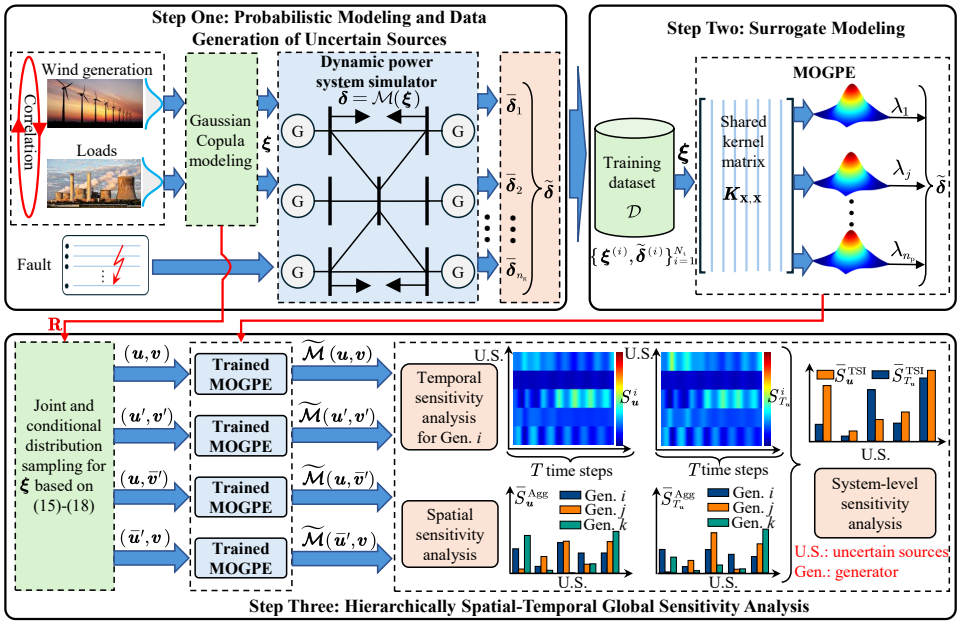

Fig. 3. Spatial-temporal global sensitivity analysis framework.

Algorithm 1: The proposed spatial-temporal global sensitivity analysis for probabilistic transient stability assessment.

Input: Recorded data of uncertain sources (e.g., wind speed and load power); the number of training data N_t; the total number of samples for sensitivity calculation N.

Output: Spatial-temporal sensitivity analysis indices: $S_{\boldsymbol{u}}^{i,t}$, $S_{T_{\boldsymbol{u}}}^{i,t}$, $\bar{S}_{\boldsymbol{u}}^{\mathrm{Agg},i}$, $\bar{S}_{T_{\boldsymbol{u}}}^{\mathrm{Agg},i}$, $\bar{S}_{\boldsymbol{u}}^{\mathrm{TSI}}$, $\bar{S}_{T_{\boldsymbol{u}}}^{\mathrm{TSI}}$.

1 Estimate the marginal distribution $\boldsymbol{\Psi}$ of wind speed and load power based on their historical data;
2 Utilize the Gaussian Copula to capture the correlation matrix $\mathbf{R}$ of uncertain sources;
3 Generate training data $\mathcal{D} = \{\boldsymbol{\xi}^{(i)}, \widetilde{\boldsymbol{\delta}}^{(i)}\}_{i=1}^{N_t}$ using LHS based on the identified Copula structure;
4 Construct MOGPE by minimizing $-\log P(\mathbf{Y} \mid \mathbf{X}, \boldsymbol{\vartheta})$ in (30) to optimize ℓ, σ^2, λ_j, and $\hat{\boldsymbol{\beta}}_{[j]}$;
5 Based on the constructed MOGPE, $S_{\boldsymbol{u}}^{i,t}$, $S_{T_{\boldsymbol{u}}}^{i,t}$, $\bar{S}_{\boldsymbol{u}}^{\mathrm{Agg},i}$, $\bar{S}_{T_{\boldsymbol{u}}}^{\mathrm{Agg},i}$, $\bar{S}_{\boldsymbol{u}}^{\mathrm{TSI}}$, and $\bar{S}_{T_{\boldsymbol{u}}}^{\mathrm{TSI}}$ are calculated via (25), (35), and (36).

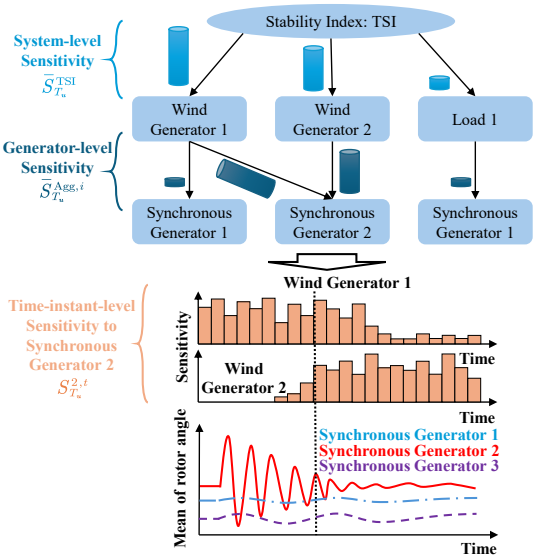

Fig. 4. An use case for utilizing the proposed global sensitivity analysis.

under uncertainties. For instance, as shown in Fig. 4, the system consists of three synchronous generators, two wind generators, and one load. Under a certain disturbance, synchronous generator 2 exhibits the largest fluctuation in the mean rotor angle, while the other synchronous generators show almost no fluctuation. The system-level global sensitivity analysis indicates that wind generators 1 and 2 have the greatest impact on overall system stability. Based on the generator-level global sensitivity analysis, it can be observed that wind generators 1 and 2 are both highly sensitive to synchronous generator 2, which is therefore identified as the key synchronous generator affecting system stability. Furthermore, the time-instant-level global sensitivity analysis reveals that wind generator 1 consistently exhibits high sensitivity to synchronous generator 2 at all times, while wind generator 2 shows zero sensitivity in the oscillation stage of the dynamics. Consequently, an additional damping controller can be designed for wind generator 2 to mitigate the rotor angle oscillations of synchronous generator 2, thereby ensuring system stability.

IV. Numerical Results

The proposed method is extensively validated on the modified IEEE 9-bus and modified NPCC 140-bus power systems. In these systems, probabilistic models are employed to represent both wind generation and load uncertainties.

1) *Wind generation uncertainty*: Wind speed is characterized by the Weibull distribution, as described in [29], with the probability density function given by:

$$\phi(\nu, m_a, m_b) = \frac{m_b}{m_a}\left(\frac{\nu}{m_a}\right)^{m_b-1} e^{-(\nu/m_a)^{m_b}}, \tag{37}$$

where ν denotes wind speed, and m_a and m_b represent the scale and shape parameters, respectively. The wind generator's output power is subsequently derived from the wind turbine's speed-power relationship:

$$P_{\mathrm{W}} = \begin{cases} 0 & (\nu < \nu_{ci} \text{ or } \nu > \nu_{co}) \\ P_{\mathrm{rated}} \cdot \frac{\nu - \nu_{ci}}{\nu_{rd} - \nu_{ci}} & (\nu_{ci} \le \nu \le \nu_{rd}) \\ P_{\mathrm{rated}} & (\nu_{rd} < \nu < \nu_{co}) \end{cases}. \tag{38}$$

Here, P_{W} is the wind generator's output power, P_{rated} is its rated power, and ν_{ci}, ν_{rd}, and ν_{co} are the cut-in, rated, and cut-out wind speeds, respectively. Wind speed samples are drawn from (37), and the corresponding power output is calculated using (38).

2) *Load uncertainty*: Consistent with prior studies, load variations are assumed to follow a Gaussian distribution [30], with the probability density expressed as:

$$\varphi(P_{\mathrm{L}}) = \frac{1}{\sqrt{2\pi}\sigma_{\mathrm{L}}} e^{-(P_{\mathrm{L}}-\mu_{\mathrm{L}})^2/(2\sigma_{\mathrm{L}}^2)}, \tag{39}$$

where P_{L} represents the load, with μ_{L} and σ_{L} being its mean and standard deviation, respectively.

In this paper, the multi-output Gaussian process emulator is implemented using PyTorch, a Python library, while PowerWorld is employed to conduct the time-domain simulations. All simulations are conducted on a laptop equipped with an AMD Ryzen 5 4600H CPU and 16 GB of RAM.

A. The Modified IEEE 9-Bus Power System

1) Accuracy Verification of MOGPE: For clarity of analysis, the proposed method is initially validated on a modified IEEE 9-bus system, as shown in Fig. 5. Two 45-MW doubly fed induction generator (DFIG)-based wind farms are connected to Bus 4 and Bus 7, referred to as Wind 4 and Wind 7, respectively. Similarly, the loads are named following the same convention. The parameters m_a and m_b for the wind speed distribution are set to 12 and 2, respectively, while μ_{L} and σ_{L} are set to the nominal load power and $0.1\mu_{\mathrm{L}}$, respectively. A three-phase short-circuit fault is applied at Bus 5 at 0.5 s and cleared at 0.6 s. For this test system, there are $n_g = 3$ synchronous generators with $T = 264$ time steps and a simulation time resolution of $\Delta t = 1/60$ s. In this subsection, the uncertain sources are assumed to be uncorrelated.

To construct the MOGPE surrogate model, the mean function is defined as $\mathbf{H}(\boldsymbol{\xi}^{(i)}) =$

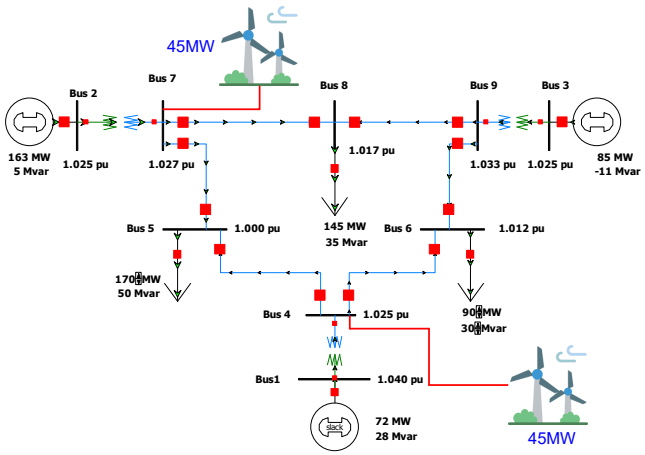

Fig. 5. The modified IEEE 9-bus power system.

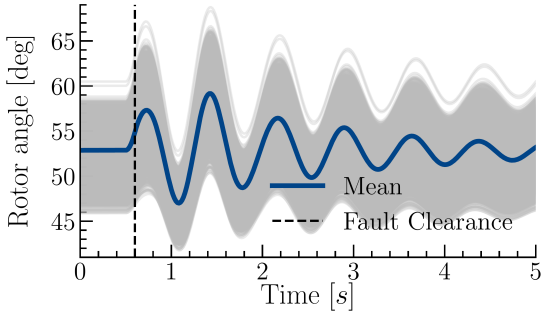

Fig. 6. True rotor angle trajectories of Generator 3 under uncorrelated uncertain sources.

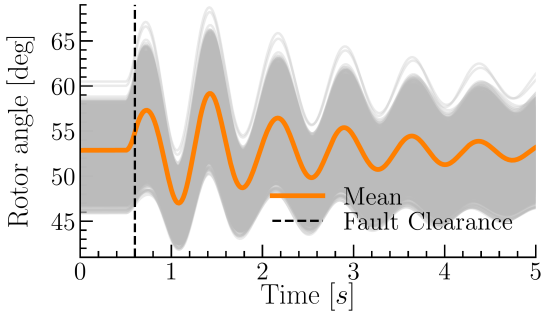

Fig. 7. Predicted rotor angle trajectories of Generator 3 under uncorrelated uncertain sources.

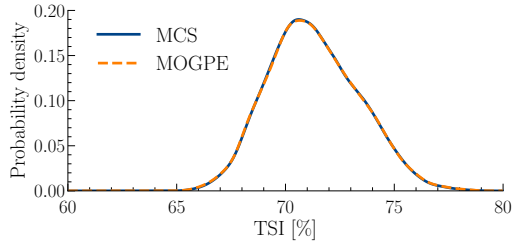

Fig. 8. True and predicted PDF of TSI for the modified IEEE 9-bus system.

$[1, \xi_1^{(i)}, \ldots, \xi_{n_u}^{(i)}, (\xi_1^{(i)})^2, \ldots, (\xi_{n_u}^{(i)})^2]$. A total of $N_t = 40$ training samples are generated using LHS, and the model is trained over $n_t = 40$ iterations. For performance evaluation, 10000 testing samples are generated via MCS. The true and predicted responses of Generator 2 are illustrated in Figs. 6 and 7, respectively. Additionally, Fig. 8 shows the probability distribution of TSI. The nearly identical distributions of the true and predicted values further validate the high accuracy of MOGPE as a surrogate model.

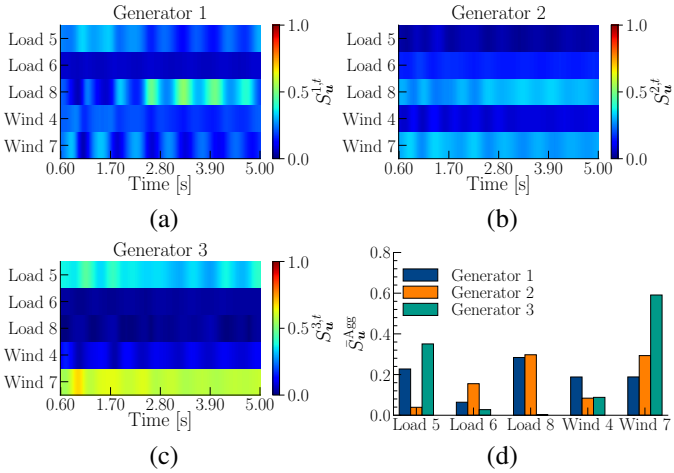

Fig. 9. First-order sensitivity index for all generators, calculated using the simulator under uncorrelated uncertain sources: (a) $S_{\boldsymbol{u}}^{i,t}$ of Generator 1; (b) $S_{\boldsymbol{u}}^{i,t}$ of Generator 2; (c) $S_{\boldsymbol{u}}^{i,t}$ of Generator 3; (4) $\bar{S}_{\boldsymbol{u}}^{\mathrm{Agg},i}$ of all generators.

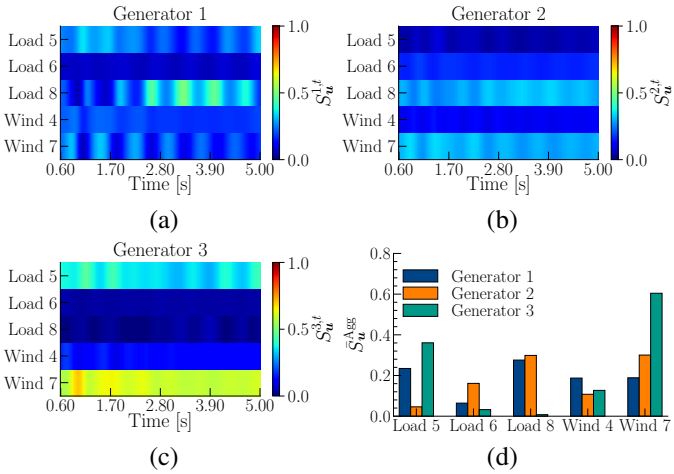

Fig. 10. First-order sensitivity index for all generators, calculated using MOGPE under uncorrelated uncertain sources: (a) $S_{\boldsymbol{u}}^{i,t}$ of Generator 1; (b) $S_{\boldsymbol{u}}^{i,t}$ of Generator 2; (c) $S_{\boldsymbol{u}}^{i,t}$ of Generator 3; (4) $\bar{S}_{\boldsymbol{u}}^{\mathrm{Agg},i}$ of all generators.

TABLE I
SENSITIVITY COMPUTATION TIME VIA THE SIMULATOR AND MOGPE.

	Simulator	MOGPE
Computation time	25.68 hours	33.39 seconds

2) Spatial-Temporal GSA Assessment: Once MOGPE is trained, it can be used to perform the spatial-temporal GSA assessment. The simulation setup is similar to that described in Section IV-A-1). N is set as 10000 to calculate each sensitivity index.

Figs. 9(a)-9(c) and 10(a)-10(c) present the heatmaps of the spatiotemporal first-order sensitivity analysis computed using the simulator and MOGPE, respectively. Similarly, Figs. 11(a)-11(c) and 12(a)-12(c) depict the heatmaps of the spatiotemporal total sensitivity analysis obtained from the simulator and MOGPE, respectively. It can be observed that MOGPE produces results consistent with the simulator, further demonstrating its accuracy. However, as shown in Table I, compared to computing these sensitivity indices using the simulator, the proposed method utilizing MOGPE achieves a speedup of 2768×. In these heatmaps, brighter colors indicate higher sensitivity values. For instance, in Fig. 11(a), Load 8 exhibits the highest total sensitivity, i.e., $S^{i,t}_{T_{\boldsymbol{u}}}$, to Generator 1 compared to other uncertain sources. However, its sensitivity is not consistently higher than that of other uncertain sources at every time step and shows greater sensitivity in the later stages of the dynamics. This indicates that Load 8 has a greater late-stage dynamic impact on the rotor angle of Generator 1. On the other hand, comparing Figs. 9(c) with 11(c), Load 5's first-order sensitivity, i.e., $S^{i,t}_{\boldsymbol{u}}$, is significantly larger than its total sensitivity, i.e., $S^{i,t}_{T_{\boldsymbol{u}}}$. This indicates that the physical interaction effects among uncertain sources are prominent and predominantly exhibit negative contributions for Generator 3. It can be also seen from Figs. 9(c) and 11(c), Load 8 exhibits positive physical interaction effects for Generator 3. We further explain why Load 5 exhibits negative interactions while Load 8 shows positive interactions for Generator 3. As illustrated in Fig. 5, compared with Load 8, Load 5 has additional connections to Generator 3 through Wind Generator 7 and Wind Generator 4. Since generators produce active power while loads consume active power, the wind generators and Load 5 play opposite roles in determining the system's power distribution, further influencing the rotor angle of Generator 3. Consequently, compared with Load 8, Load 5 exhibits stronger negative interactions with other uncertain sources with respect to the rotor angle of Generator 3. However, Load 8 has no wind generation in its connection path to Generator 3, leading to stronger positive interactions.

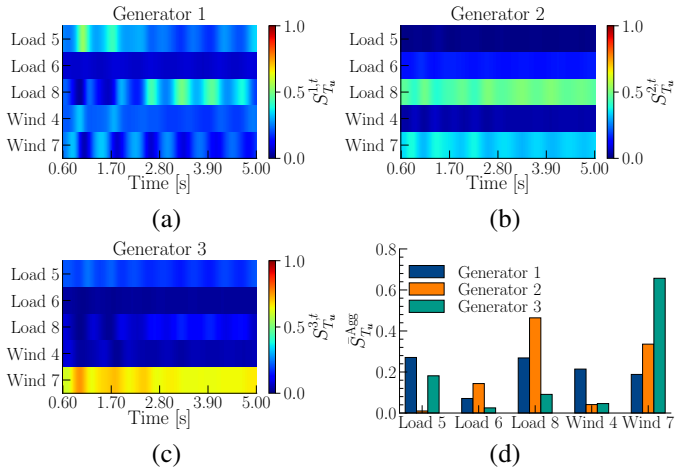

Fig. 11. Total sensitivity index for all generators, calculated using the simulator under uncorrelated uncertain sources: (a) $S^{i,t}_{T_{\boldsymbol{u}}}$ of Generator 1; (b) $S^{i,t}_{T_{\boldsymbol{u}}}$ of Generator 2; (c) $S^{i,t}_{T_{\boldsymbol{u}}}$ of Generator 3; (d) $\bar{S}^{\text{Agg},i}_{T_{\boldsymbol{u}}}$ of all generators.

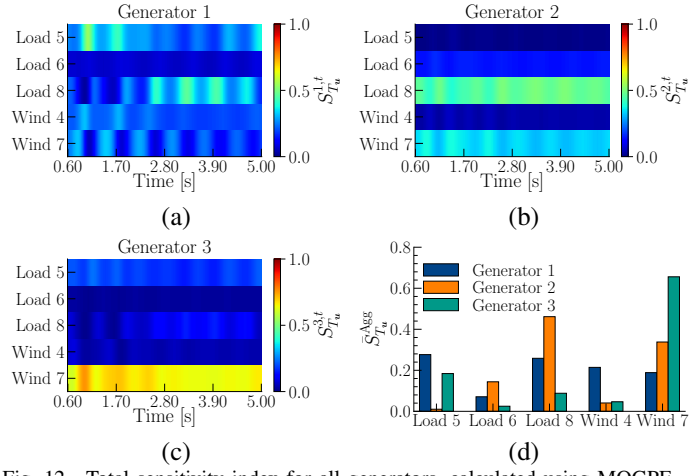

Fig. 12. Total sensitivity index for all generators, calculated using MOGPE under uncorrelated uncertain sources: (a) $S^{i,t}_{T_{\boldsymbol{u}}}$ of Generator 1; (b) $S^{i,t}_{T_{\boldsymbol{u}}}$ of Generator 2; (c) $S^{i,t}_{T_{\boldsymbol{u}}}$ of Generator 3; (d) $\bar{S}^{\text{Agg},i}_{T_{\boldsymbol{u}}}$ of all generators.

Figs. 9(d) and 10(d) present the calculated $\bar{S}^{\text{Agg},i}_{\boldsymbol{u}}$ using both the simulator and MOGPE. Figs. 11(d) and 12(d) present $\bar{S}^{\text{Agg},i}_{T_{\boldsymbol{u}}}$ using both the simulator and MOGPE. The results demonstrate a high degree of consistency between the two methods. Comparing Figs. 9(d) and Fig. 11(d), it is evident that $\bar{S}^{\text{Agg},i}_{\boldsymbol{u}}$ and $\bar{S}^{\text{Agg},i}_{T_{\boldsymbol{u}}}$ vary across different uncertain sources. This observation aligns with the heatmap analysis, further confirming the presence of physical interaction effects among uncertain sources. Additionally, as seen in Figs. 9(d) and Fig. 11(d), the sensitivity of different generators to the same uncertain sources is not identical. To determine whether $\bar{S}^{\text{Agg},i}_{\boldsymbol{u}}$ or $\bar{S}^{\text{Agg},i}_{T_{\boldsymbol{u}}}$ is more suitable for evaluating the impact of uncertain sources in PTSA, this study fixes the power output of each uncertain source at its nominal value while performing MCS on the remaining uncertain sources, as shown in Table II. Case 1 represents the scenario without fixing any input, and the variance of each generator's rotor angle is plotted in Fig. 13. In each case, if the variance of a generator's rotor angle is closer to that in Case 1, it implies that the fixed input in this case has lower sensitivity to the generator's rotor angle dynamics. Observations indicate that the sensitivity trend reflected by $\bar{S}^{\text{Agg},i}_{T_{\boldsymbol{u}}}$ aligns with the trend in variance differences between each case and Case 1, as depicted in Fig. 13, whereas $\bar{S}^{\text{Agg},i}_{\boldsymbol{u}}$ does not capture this trend. For example, in Fig. 13(b), Case 4 exhibits the largest variance difference compared to Case 1, consistent with the ranking of $\bar{S}^{\text{Agg},2}_{T_{\boldsymbol{u}}}$ in Figs. 11(d) and 12(d) present $\bar{S}^{\text{Agg},i}_{T_{\boldsymbol{u}}}$, but inconsistent with $\bar{S}^{\text{Agg},2}_{\boldsymbol{u}}$ in Figs. 9(d) and 10(d). Thus, the total sensitivity index $\bar{S}^{\text{Agg},i}_{T_{\boldsymbol{u}}}$ provides

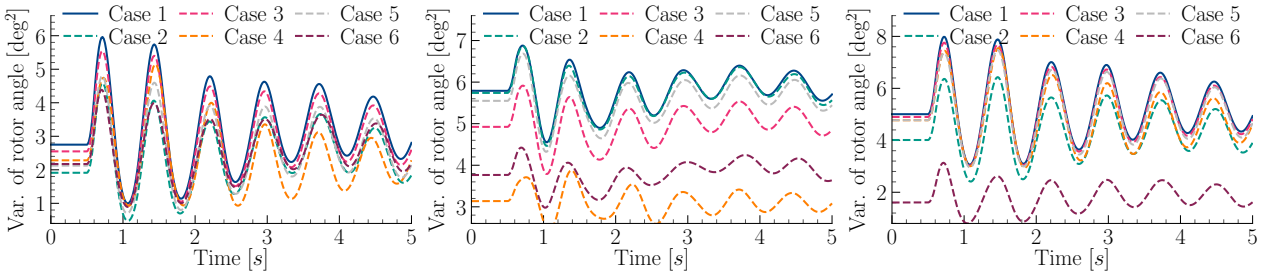

Fig. 13. Variance (Var.) of rotor angle for all generators under different cases.: (a) Generator 1; (b) Generator 2; (c) Generator 3.

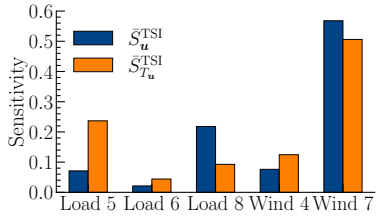

Fig. 14. $\bar{S}_{\boldsymbol{u}}^{\text{TSI}}$ and $\bar{S}_{T_{\boldsymbol{u}}}^{\text{TSI}}$ of each uncertain sources

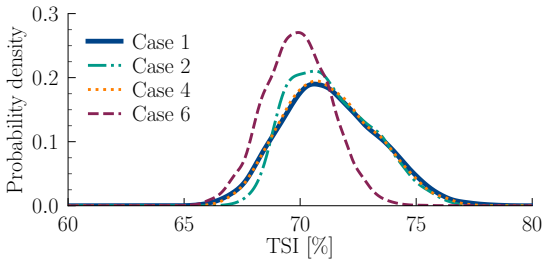

Fig. 15. PDF of TSI under different cases.

TABLE II
DIFFERENT CASES OF FIXING UNCERTAIN SOURCES

Cases	Case 1	Case 2	Case 3	Case 4	Case 5	Case 6
Fixed U.S.[a]	None	Load 5	Load 6	Load 8	Wind 4	Wind 7

[a] U.S.: Uncertain sources

a more accurate description of global sensitivity for each generator and it can assist system operators in determining which uncertain sources should be adjusted to regulate the rotor angle dynamics of specific generators.

3) System-Level GSA for TSI: In this subsection, the simulation setup is similar to that in Section IV-A-1). Fig. 14 illustrates the PDFs of TSI under different cases. Results show that fixing uncertain sources with higher $\bar{S}_{T_{\boldsymbol{u}}}^{\text{TSI}}$ leads to larger deviations from the reference scenario (Case 1, all uncertain sources vary). Conversely, fixing sources based on higher $\bar{S}_{\boldsymbol{u}}^{\text{TSI}}$ does not follow this trend. For example, in Fig. 15, Case 4 (fixing Load 8) shows a much smaller deviation from Case 1 compared to Case 2, despite Load 8 having a higher $\bar{S}_{\boldsymbol{u}}^{\text{TSI}}$ than Load 5. Thus, $\bar{S}_{T_{\boldsymbol{u}}}^{\text{TSI}}$ is a more effective metric for evaluating the significance of uncertain sources in PTSA, as it captures the interactions among these sources.

4) GSA under Different Distribution Correlations: This subsection analyzes how changes in the correlation between uncertain sources influence $\bar{S}_{\boldsymbol{u}}^{\text{Agg},i}$, $\bar{S}_{T_{\boldsymbol{u}}}^{\text{Agg},i}$, $\bar{S}_{\boldsymbol{u}}^{\text{TSI}}$, and $\bar{S}_{T_{\boldsymbol{u}}}^{\text{TSI}}$. The simulation setup remains consistent with Section IV-A-1), except that Load 5 and Load 8 are assigned different correlation coefficients.

Figs. 16 and 17 illustrate the values of $\bar{S}_{\boldsymbol{u}}^{\text{Agg},i}$, $\bar{S}_{T_{\boldsymbol{u}}}^{\text{Agg},i}$, $\bar{S}_{\boldsymbol{u}}^{\text{TSI}}$, and $\bar{S}_{T_{\boldsymbol{u}}}^{\text{TSI}}$ for all generators at various correlation coefficients. Sensitivity patterns differ among generators as the correlation coefficient changes. Notably, as the correlation between Load 5 and Load 8 increases, their corresponding $\bar{S}_{\boldsymbol{u}}^{\text{Agg},i}$ values consistently rise, indicating an increased shared variance contribution. Furthermore, the differences between $\bar{S}_{\boldsymbol{u}}^{\text{Agg},i}$ and $\bar{S}_{T_{\boldsymbol{u}}}^{\text{Agg},i}$ for Loads 5 and 8, representing physical interaction effects, also change with correlation. In contrast, sensitivity indices of other uncorrelated uncertain sources remain largely unaffected. These findings demonstrate that changes in correlation significantly influence the sensitivity indices.

5) GSA under Different Fault Severities: To investigate how the sensitivity indices vary with fault duration and severity, we scan the fault duration t_d from 0.05 s to 0.3 s. Taking Generator 3 as an example, its sensitivity heatmaps for the two indices are shown in Fig. 18. It can be seen that the total sensitivity $S_{T_{\boldsymbol{u}}}^{3,t}$ does not increase monotonically with fault duration. The results also suggest that there is a critical fault duration beyond which the sensitivity patterns fundamentally change. For example, Wind 7's $S_{T_{\boldsymbol{u}}}^{i,t}$ first increase with fault duration but begin to decrease once $t_d = 0.25$ s. This may be because when the fault duration or severity is small, Wind 7 has large impacts on the system response, and its sensitivity increases as the fault severity grows. However, when the fault duration or severity becomes sufficiently large, the fault itself becomes the dominant factor affecting system stability, and the impact of Wind 7 on the dynamic response may change.

B. NPCC 140-Bus Power System

The proposed method is validated using the modified NPCC 140-bus power system, comprising 78 loads. Five synchronous generators at Buses 23, 48, 57, 71, and 122 are substituted with DFIG-based wind farms of equivalent capacity, resulting in 83 uncertain sources. The simulation configuration aligns with Section IV-A-1), except that a three-phase short-circuit fault is introduced at Bus 8 at 0.5 s and cleared at 0.6 s. For this test system, there are $n_g = 43$ synchronous generators with $T = 264$ time steps and a simulation time resolution of $\Delta t = 1/60$ s. A total of $N_{\text{t}} = 400$ training samples are generated using LHS to construct the MOGPE model. Loads in Region 1 (Buses 11, 12, 14), Region 2 (Buses 53, 55, 59),

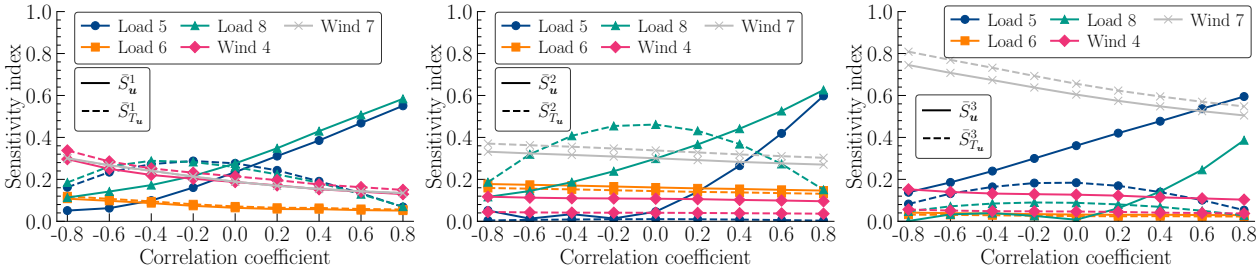

Fig. 16. $\bar{S}_{\boldsymbol{u}}^{\text{Agg},i}$ and $\bar{S}_{T_{\boldsymbol{u}}}^{\text{Agg},i}$ for all generators under different correlation coefficients: (a) Generator 1; (b) Generator 2; (c) Generator 3.

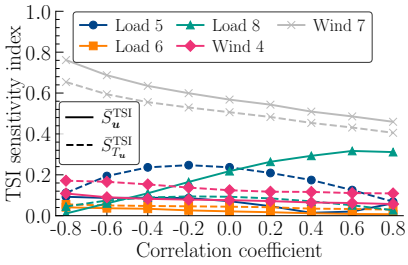

Fig. 17. $\bar{S}_{\boldsymbol{u}}^{\text{TSI}}$ and $\bar{S}_{T_{\boldsymbol{u}}}^{\text{TSI}}$ under different correlation coefficients.

and Region 3 (Buses 89, 90, 91), along with wind generation in Region 2 (Buses 48, 57, 71), are assigned a correlation coefficient of 0.4. Uncertain sources across distinct regions are assumed to be independent. The sample size N is set to 20000 for computing each sensitivity index.

Fig. 19 presents the mean and variance of the true and predicted rotor angle trajectories for all generators under MCS. It can be observed that the MOGPE predictions closely match the true values, thereby demonstrating the scalability of MOGPE for surrogate modeling in large-scale dynamic power systems. By using MOGPE, the proposed GSA scheme achieves approximately a 1983-fold speed-up, as shown in Table III. Fig. 20 shows the total aggregated sensitivity $\bar{S}_{T_{\boldsymbol{u}}}^{\text{TSI}}$ corresponding to each uncertain source. It is observed that most uncertain sources exhibit near-zero sensitivity with respect to the TSI. In this study, the uncertain sources with the highest $\bar{S}_{T_{\boldsymbol{u}}}^{\text{TSI}}$ values—cumulatively accounting for 99% of the total sensitivity—are selected as the final input variables for MCS analysis, resulting in a total of 48 most influential uncertain sources. As illustrated in Fig. 21, conducting probabilistic transient stability assessment using only these 48 most influential uncertain sources yields results that closely match those obtained using all uncertain sources. This validates the effectiveness of the proposed sensitivity analysis and demonstrates its capability to significantly enhance the computational efficiency of PTSA, while also assisting system operators in focusing on the most critical influencing factors.

TABLE III
SENSITIVITY COMPUTATION TIME VIA THE SIMULATOR AND MOGPE.

	Simulator	MOGPE
Computation time	1368.72 hours	0.69 hours

C. Discussions

- **Determination of the Amount of the Required Samples:** The proposed MOGPE uses only three hyperparameters for each output, ℓ, σ^2, and λ_j, which correspond to the kernel length-scale, noise variance, and scaling coefficient, respectively. In theory, at least three data points are sufficient to identify these three hyperparameters. However, in practice, the required number of training samples for MOGPE also depends on the input dimensionality [31], ensuring that each dimension is adequately sampled. Therefore, the number of training samples should exceed the input dimensionality. Through grid search, we found that using a sample size N_t greater than approximately four times the input dimension yields satisfactory prediction accuracy. In the future, active learning strategies can be employed for the proposed MOGPE to reduce the required number of training samples. This is because they prioritize sampling in regions where the model is most uncertain or where system behavior changes rapidly, such as near stability boundaries. Each new sample contributes the most informative data, enabling faster accuracy improvement. Moreover, it avoids allocating samples to regions that the model already captures well, thereby reducing redundancy and lowering the total number of training points needed for reliable predictions.
- **MOGPE Adaptation:** If the fault type or location changes, the MOGPE can be updated via transfer learning to accelerate model adaptation and thereby improve assessment efficiency. On one hand, the proposed MOGPE requires only three hyperparameters for each output, namely the kernel function length scale, noise variance, and scaling factor, which theoretically means that only a very small number of training samples (at least three data points) are sufficient for updating the MOGPE. On the other hand, transfer learning can provide a good initial point (close to a well-trained model), further reducing the number of samples needed to train the MOGPE. This data efficiency is particularly valuable in large-scale power systems.
- **Impacts under Non-Gaussian Tails or Nonlinear Dependency:** The global sensitivity index proposed in this paper involves sampling from the conditional probability distributions of correlated input variables. The Gaussian copula conveniently facilitates this task by leveraging the properties of the Gaussian function to describe condi-

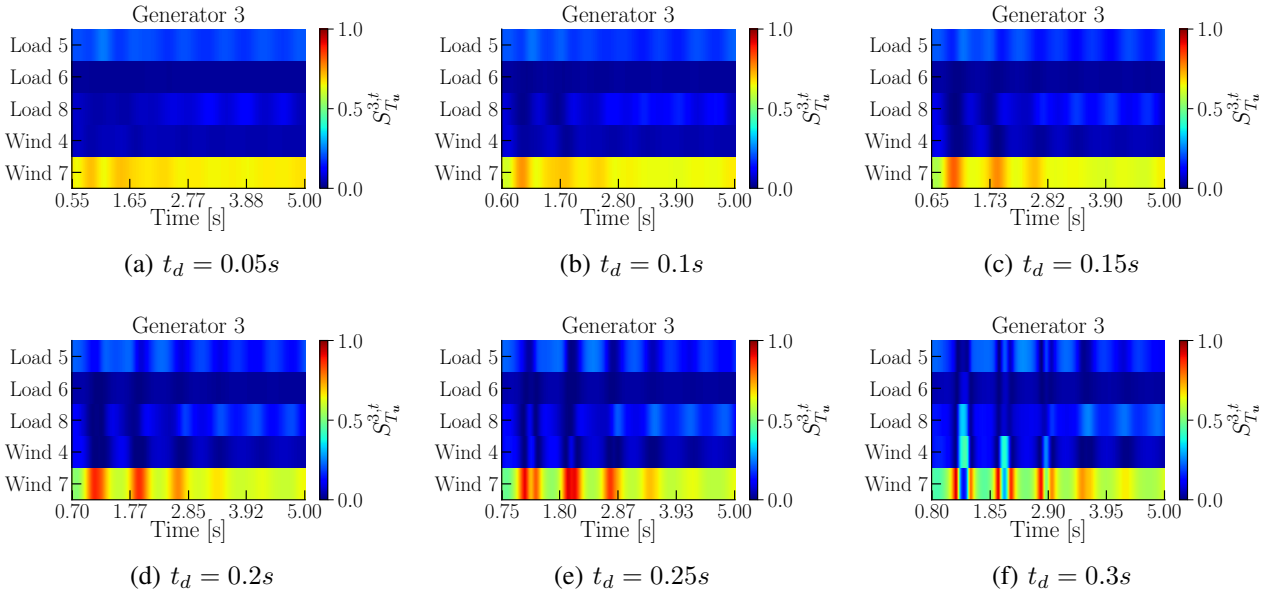

Fig. 18. The total sensitivity $S^{3,t}_{T_u}$ of Generator 3 under different fault durations t_d.

tional correlations. However, it cannot capture heavy-tailed distributions or nonlinear dependencies. Vine copulas can model such uncertainties, but they cannot naturally describe the conditional probability distributions of correlated input variables. Future work will explore the use of Vine copulas to enable conditional probability distribution sampling of correlated input variables.

V. Conclusion

In this paper, a spatial-temporal GSA method is proposed for PTSA. Several GSA indices are developed to hierarchically evaluate the sensitivity between the spatiotemporal responses of generator trajectories and uncertain sources in dynamic power systems. To efficiently compute these indices, a computationally efficient multi-output surrogate model, namely MOGPE, is developed to replace the time-consuming time-domain simulator. Numerical results demonstrate the effectiveness and scalability of the proposed method. The following conclusions can be drawn:

- MOGPE significantly improves the efficiency of dynamic power system simulations and exhibits strong scalability. For example, by using MOGPE, the spatial-temporal global sensitivity analysis achieves up to a 1983× speed-up for the NPCC 140-bus power system;
- Compared to the first-order sensitivity index, the total sensitivity index is more suitable for GSA as it accounts for the physical interactions among uncertain sources;
- The proposed spatial-temporal GSA scheme effectively identifies the key influential factors impacting PTSA.

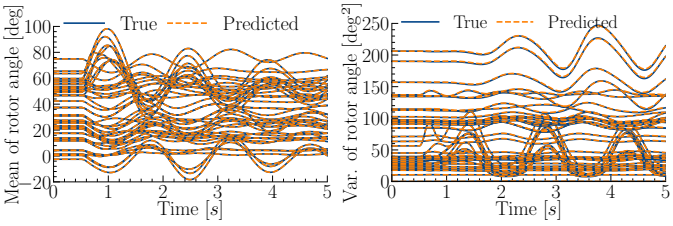

Fig. 19. True and predicted rotor angle trajectories of all generators under MCS. (a) Mean; (b) Variance.

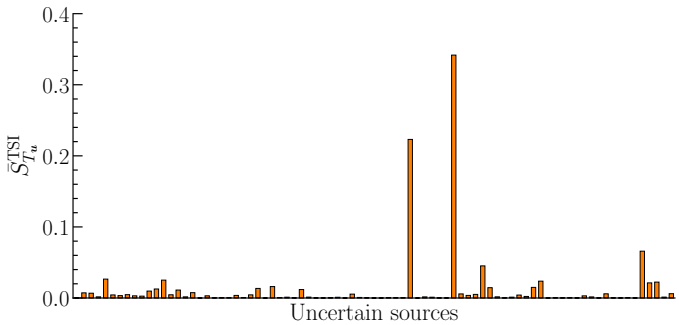

Fig. 20. $\bar{S}^{\text{TSI}}_{T_u}$ for NPCC 140-bus power system

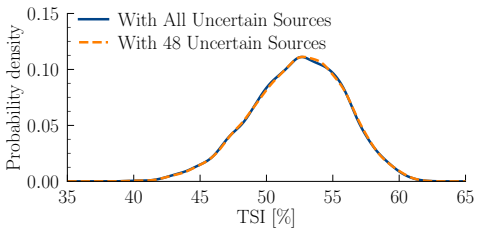

Fig. 21. Distribution of TSI using different uncertain sources as inputs.

References

[1] B. Tan, J. Zhao, M. Netto, V. Krishnan, V. Terzija, and Y. Zhang, "Power system inertia estimation: Review of methods and the impacts of converter-interfaced generations," *Int. J. Electr. Power Energy Syst.*, vol. 134, p. 107362, 2022.

[2] C. He, H. Geng, K. Rajashekara, and A. Chandra, "Analysis and control of frequency stability in low-inertia power systems: A review," *IEEE/CAA J. Autom. Sinica*, vol. 11, no. 12, pp. 2363–2383, 2024.

[3] B. Tan and J. Zhao, "Debiased uncertainty quantification approach for probabilistic transient stability assessment," *IEEE Trans. Power Syst.*, vol. 38, no. 5, pp. 4954–4957, 2023.

[4] R. Fatah Mochamad, R. Preece, and K. N. Hasan, "Probabilistic multi-stability operational boundaries in power systems with high penetration of power electronics," *Int. J. Electr. Power Energy Syst.*, vol. 135, p. 107382, 2022.

[5] M. Abapour and M.-R. Haghifam, "Probabilistic transient stability assessment for on-line applications," *Int. J. Electr. Power Energy Syst.*, vol. 42, no. 1, pp. 627–634, 2012.

[6] K. Ye, J. Zhao, H. Li, and M. Gu, "A high computationally efficient parallel partial Gaussian process for large-scale power system probabilistic transient stability assessment," *IEEE Trans. Power Syst.*, vol. 39, no. 2, pp. 4650–4660, 2024.

[7] Y. Liu, J. Wang, and Z. Yue, "Improved multi-point estimation method based probabilistic transient stability assessment for power system with wind power," *Int. J. Electr. Power Energy Syst.*, vol. 142, p. 108283, 2022.

[8] R. Preece and J. V. Milanović, "Assessing the applicability of uncertainty importance measures for power system studies," *IEEE Trans. Power Syst.*, vol. 31, no. 3, pp. 2076–2084, 2016.

[9] K. N. Hasan, R. Preece, and J. V. Milanović, "Priority ranking of critical uncertainties affecting small-disturbance stability using sensitivity analysis techniques," *IEEE Trans. Power Syst.*, vol. 32, no. 4, pp. 2629–2639, 2017.

[10] C. Qin, Y. Jin, M. Tian, P. Ju, and S. Zhou, "Comparative study of global sensitivity analysis and local sensitivity analysis in power system parameter identification," *Energies*, vol. 16, no. 16, p. 5915, Aug. 2023.

[11] B. Qi, K. N. Hasan, and J. V. Milanović, "Identification of critical parameters affecting voltage and angular stability considering load-renewable generation correlations," *IEEE Trans. Power Syst.*, vol. 34, no. 4, pp. 2859–2869, 2019.

[12] T. Homma and A. Saltelli, "Importance measures in global sensitivity analysis of nonlinear models," *Reliab. Eng. Syst. Saf.*, vol. 52, no. 1, pp. 1–17, 1996.

[13] X. Xu, Z. Yan, M. Shahidehpour, H. Wang, and S. Chen, "Power system voltage stability evaluation considering renewable energy with correlated variabilities," *IEEE Trans. Power Syst.*, vol. 33, no. 3, pp. 3236–3245, 2018.

[14] F. Ni, M. Nijhuis, P. H. Nguyen, and J. F. G. Cobben, "Variance-based global sensitivity analysis for power systems," *IEEE Trans. Power Syst.*, vol. 33, no. 2, pp. 1670–1682, 2018.

[15] I. Azzini, T. A. Mara, and R. Rosati, "Comparison of two sets of monte carlo estimators of sobol' indices," *Environ. Modell. Softw.*, vol. 144, p. 105167, 2021.

[16] Y. Li, Y. Xu, S. Yao, S. Lu, W. Gu, L. Mili, and M. Korkali, "Global sensitivity analysis for integrated heat and electricity energy system," *IEEE Trans. Power Syst.*, pp. 1–14, 2024.

[17] F. Ni, M. Nijhuis, P. H. Nguyen, and J. F. G. Cobben, "Variance-based global sensitivity analysis for power systems," *IEEE Trans. Power Syst.*, vol. 33, no. 2, pp. 1670–1682, 2018.

[18] S. Peng, X. Lin, J. Tang, K. Xie, F. Ponci, and A. Monti, "A set of novel global sensitivity analysis indices for probabilistic static voltage stability assessment with correlated uncertainty sources," *IEEE Trans. Power Syst.*, vol. 39, no. 2, pp. 2543–2557, 2024.

[19] H. Wang, Z. Yan, M. Shahidehpour, X. Xu, and Q. Zhou, "Quantitative evaluations of uncertainties in multivariate operations of microgrids," *IEEE Trans. Smart Grid*, vol. 11, no. 4, pp. 2892–2903, 2020.

[20] K. Ye, J. Zhao, F. Ding, R. Yang, X. Chen, and G. W. Dobbins, "Global sensitivity analysis of large distribution system with PVs using deep Gaussian process," *IEEE Trans. Power Syst.*, vol. 36, no. 5, pp. 4888–4891, 2021.

[21] K. Ye, J. Zhao, C. Huang, N. Duan, Y. Zhang, and T. E. Field, "A data-driven global sensitivity analysis framework for three-phase distribution system with PVs," *IEEE Trans. Power Syst.*, vol. 36, no. 5, pp. 4809–4819, 2021.

[22] B. Tan, T. Su, Y. Weng, K. Ye, P. Pareek, P. Vorobev, H. Nyugen, J. Zhao, and D. Deka, "Gaussian processes in power systems: Techniques, applications, and future works," *Applied Energy*, 2025.

[23] O. Garcia-Cabrejo and A. Valocchi, "Global sensitivity analysis for multivariate output using polynomial chaos expansion," *Reliability Engineering & System Safety*, vol. 126, pp. 25–36, 2014.

[24] S. S. Shaukat, T. A. Rao, and M. A. Khan, "Impact of sample size on principal component analysis ordination of an environmental data set: Effects on eigenstructure," *Ekológia*, vol. 35, no. 2, p. 173, 2016.

[25] S. Kucherenko, S. Tarantola, and P. Annoni, "Estimation of global sensitivity indices for models with dependent variables," *Comput. Phys. Commun.*, vol. 183, no. 4, pp. 937–946, 2012.

[26] L. Xu, Z. Lu, and S. Xiao, "Generalized sensitivity indices based on vector projection for multivariate output," *Appl. Math. Model.*, vol. 66, pp. 592–610, 2019.

[27] Y. Xu, L. Mili, M. Korkali, K. Karra, Z. Zheng, and X. Chen, "A data-driven nonparametric approach for probabilistic load-margin assessment considering wind power penetration," *IEEE Trans. Power Syst.*, vol. 35, no. 6, pp. 4756–4768, 2020.

[28] R. B. Nelsen, *An Introduction to Copulas*, 2nd ed., ser. Springer Series in Statistics. New York: Springer, 2006.

[29] W. C. Wong and C. Y. Chung, "Coordinated damping control design for DFIG-based wind generation considering power output variation," *IEEE Trans. Power Syst.*, vol. 27, no. 4, pp. 1916–1925, 2012.

[30] R. Billinton and D. Huang, "Effects of load forecast uncertainty on bulk electric system reliability evaluation," *IEEE Trans. Power Syst.*, vol. 23, no. 2, pp. 418–425, 2008.

[31] M. Hoang, N. Hoang, H. Pham, and D. Woodruff, "Revisiting the sample complexity of sparse spectrum approximation of Gaussian processes," *Advances in Neural Information Processing Systems*, vol. 33, pp. 12 710–12 720, 2020.